

Angular reconstitution-based 3D reconstructions of nano-molecular structures from super-resolution light-microscopy images

Desirée Salas^{1,a}, Antoine Le Gall^{1,a}, Jean-Bernard Fiche^a, Alessandro Valeri^a, Yonggang Ke^c, Patrick Bron^a, Gaetan Bellot^{2,b}, Marcelo Nollmann^{2,b}

^a Centre de Biochimie Structurale, CNRS, INSERM, Université de Montpellier, 34090 Montpellier, France;

^b Institut de Génomique Fonctionnelle, CNRS UMR5203, INSERM U1191, Université de Montpellier, 34090 Montpellier, France.

^c Wallace H. Coulter Department of Biomedical Engineering, Georgia Institute of Technology and Emory University, Atlanta, Georgia 30322, USA.

¹ These authors contributed equally to this work.

²To whom correspondence should be addressed: marcelo.nollmann@cbs.cnrs.fr;
gaetan.bellot@igf.cnrs.fr

Abstract

Super-resolution light microscopy allows the imaging of labelled supramolecular assemblies at a resolution surpassing the classical diffraction limit. A serious limitation of the super-resolution approach is sample heterogeneity and the stochastic character of the labelling procedure. To increase the reproducibility and the resolution of the super-resolution results, we apply multivariate statistical analysis methods and three-dimensional reconstruction approaches originally developed for cryogenic electron microscopy of single particles. These methods allow for the reference-free 3D reconstruction of nano-molecular structures from two-dimensional super-resolution projection images. Since these 2D projection images all show the structure in high-resolution directions of the optical microscope, the resulting 3D reconstructions have the best possible, isotropic, resolution in all directions.

Significance

Super-resolution imaging techniques have become an essential tool to study the organization and structure of biological molecules with previously unimagined detail. It is becoming clear, however, that structural heterogeneity, dynamics, and low labeling densities can impede the potential of such technologies. Here, we describe a model-free method based on single-particle reconstruction algorithms to extract 3D isotropic structural information from 2D super-resolution images of nanometer-sized supramolecular structures, such as DNA origami or protein complexes. We expect our work will help bridge the gap between super-resolution microscopy and conventional electron microscopy.

\body

Introduction

With recent advances in electron detection and image processing, electron microscopy (EM) now enables the exploration of supramolecular architectures at nanoscale resolutions (1–3). The resolution in conventional fluorescence light microscopies is limited by diffraction to a few hundred nanometers. Recently, several super-resolution microscopy methods were developed to surpass the intrinsic resolution limit of conventional fluorescence microscopy (4). Uniquely, super-resolution microscopies enable imaging of man-made materials and biological objects in complex environments with chemical specificity and previously unimagined detail (5–7). However, the dissection of structural heterogeneity, dynamics and low labeling densities, most noticeable at the nano-scale, limit the full potential of current super-resolution analysis methods.

Recently, single-particle averaging approaches were successfully applied to super-resolution optical microscopy images to unravel ultrastructural details of the nuclear pore complex (8), the ESCRT machinery at HIV assembly sites (6), and the machinery of the centrosome (9). Typically, these methods relied on the use of structural templates to seed the reconstruction process and used cylindrical or spherical symmetries to reveal information on the radial distribution of components within complexes. These approaches are thus not easily transferable to *de novo* systems and may lead to structures that are biased towards those of templates.

Here, we present a model-free method adapted from conventional Electron Microscopy Single-Particle Reconstruction (EM SPR) algorithms to extract 3D isotropic structural information from 2D Single-Molecule Localization Microscopy (SMLM) (10) images of supramolecular structures. We demonstrate the applicability of this method by solving the 3D structures of DNA origami (11, 12) and of simulated large protein complexes.

Results

Super-resolution imaging of model DNA origami

DNA origami were labelled by DNA-PAINT (13, 14). Equally-spaced ‘docking’ strands were placed to provide high-density labeling using Atto647n- or Alexa488-labeled ‘imager’ strands (Fig. 1A, and SI Appendix, Figs. S1, S3, and Materials and Methods). Two distinct DNA

origami structures were used to demonstrate our approach on 1D and 3D architectures: a linear rod of 165 nm in length and a tetrahedron of 110 nm edge length (14) (Figs. 1C-D, and SI Appendix, Figs. S1-4). Linear rods were immobilized on a flat biotin-PEG surface by specific biotin-neutravidin-biotin-PEG interactions at the two extremities along the long axis, thus most rods laid flat on the surface (SI Appendix, Fig. S5B). Tetrahedrons were immobilized by non-specific interactions with a rough poly-L-lysine surface, ensuring random orientations with respect to the optical axis (SI Appendix, Fig. S5C).

After surface immobilization, we performed DNA-PAINT imaging in a microfluidics chamber (SI Appendix, Fig. S5). For each structure, thousands of monodisperse single DNA origami particles were obtained by DNA-PAINT at a localization precision of 15 ± 3 nm (Fig. 1B, and SI Appendix Fig. S6, and Materials and Methods) covering 153 nm of the rod length and the full 110 nm of the tetrahedron side.

Single-particle 3D reconstructions from single-molecule datasets

Localizations from single particles were converted to images by calculating the probability density of localization. The labeling spacing (7 nm) was lower than the localization precision (15 nm, SI Appendix, Fig. S6). Images from single-particles were aligned and classified into class averages by Multivariate Statistical Analysis (MSA) classification. Well-defined class averages were then selected as references for Multi-Reference Alignment (MRA), followed by resubmission to MSA classification (15). After a small number of iterative cycles (typically ~5) of MRA and MSA classification, class averages did not evolve. Class averages were obtained from the sum of images representing particles in the same orientation, resulting in a more uniformly distributed fluorescence signal than that of raw particles, and leading to overall better projections (Figs. 1C-D, and SI Appendix, Figs. S7-8, and Materials and Methods).

The best class averages were used to compute 3D reconstructions using the angular reconstitution method (SI Appendix, Fig. S9) (16). This technique uses the data in the projection images to find the relative spatial orientations of the projection images without using any instrumentally-driven projection direction. These orientations are then used to derive a 3D model. Strikingly, both DNA origami structures could be successfully reconstructed from 5427 and 2219 individual particles without relying on initial models (Fig. 2B). We then performed 3D reconstructions using theoretical models of DNA origami. Reconstructions with or without initial models yielded very similar 3D structures (SI Appendix, Figs. S10-11 and Figs. 2A-BE-F, respectively), supporting the robustness of the reconstruction method without an initial 3D template.

This method was robust with respect to total particle number, localization precision of single events, the density of localizations, and background levels (SI Appendix, Fig. S13). To further assess the robustness of reconstructions, we split raw particles into two sets and calculated the correlation between the final reconstructions obtained from each set of particles as a function of resolution using Fourier Shell Correlation (FSC, Fig. 2C, and SI Appendix, Fig. S11) (17). The FSC is the correlation between two independent structures, where each structure is calculated from half the images. The resolution of the reconstructions was estimated using the criterium of Rosenthal et al. (18) and resulted in 18 ± 2 and 50 ± 4 nm for the linear rod and tetrahedron, respectively (Fig. 2C). Fourier Ring Correlation (FRC)

(19), which applies the computational principles of FSC to two-dimensional datasets, was used to evaluate the resolution gain obtained with 3D reconstructions on DNA-PAINT localization data. Averaging 100 FRC curves corresponding to single linear rod and tetrahedron localization datasets yielded resolutions of 22 ± 9 and 22 ± 10 nm, respectively (Figs. 2D and SI Appendix, Fig. S12). The lateral resolution in DNA-PAINT (or other SMLM methods) is 2-3 times better than the axial resolution, leading to the acquisition of 3D volumes with anisotropic resolutions. Notably, our 3D reconstructions displayed isotropic resolution as the detection method relies on the use of 2D super-resolution projection images that have the best resolution attainable by SMLM.

Additionally, direct measurements of each 3D structure were compared to theoretical predictions. For the linear rod, lengths were 161 ± 8 and 153 ± 5 nm (mean \pm interquartile range, Fig. 2E) for the reconstruction and the model, respectively. Similar agreements were found in the lengths of the tetrahedron (126 ± 11 and 122 ± 5 nm, Fig. 2E). Further validation of 3D reconstructions was made by computing their FSC against reference 3D models, resulting in 23 nm for the linear rod and 35 nm for the tetrahedron (SI Appendix, Fig. S11). Overall, these data suggest that the reconstructions were highly accurate and recovered the 3D structure of the model.

3D reconstructions of large protein complexes from simulated datasets

To test whether this method was applicable to reconstruct the ultrastructures of large protein complexes, we produced a high-resolution structural model of the T4 bacteriophage (Fig. 3A, inset) and applied the single-particle reconstruction algorithm to retrieve 3D reconstructions from simulated single-molecule localization microscopy (SMLM) experiments. We investigated the robustness of the method with respect to labeling density by reconstructing the model from very high (6 nm average distance between emitters, Fig. 3B, left panel) to extremely low-labeling density SMLM datasets (~48 nm between emitters, Fig. 3E, left panel). Strikingly, reconstructions were successful across the whole range of densities tested (Figs. 3B-E, and SI Appendix, Fig. S14). Robustness of the reconstructions was assessed by performing the FSC of single-particles 3D reconstructions against the high-resolution theoretical model and by calculating Euler angle distributions (Fig. 3A and SI Appendix, Fig. S14). Reconstructions were robust even when the average distance between labeling sites was considerably larger than the localization precision, and comparable to the size of the object itself (Figs. 3A, 3E). At these low densities, the original shape of the object was hardly recognizable from individual raw particles, but the stochasticity of labeling sites combined with single-particle classification and averaging led to properly reconstructed classes and successful 3D reconstructions (Figs. 3E and SI Appendix, Fig. S14). Similar results were observed when a model was used as a template (SI Appendix, Fig. S15).

Next, we tested the robustness of this approach to noise contamination and decreasing specific labeling densities to simulate realistic experimental conditions. Most notably, SMLM based on the use of fluorescently-labeled antibodies can contain a considerable proportion of non-specific localizations. Thus, we generated various densities of contaminating localizations in conjunction with reduced specific labeling densities. With a single cycle of MRA and MSA classification, class averages of the most distinct structure orientations could be successfully retrieved without a model and at high signal to noise ratios

in all tested conditions (SI Appendix, Fig. S16). Multivariate Statistical Analysis classification is thus very robust to noise contamination by background emitters typically obtained with light microscopy approaches. Overall, these simulations strongly suggest that our method will be able to reconstruct large protein complexes from experimental SMLM datasets.

3D reconstructions of asymmetric structures from simulated datasets

Finally, we investigated the effect of symmetry in 3D reconstructions. To this end, we first reconstructed the structures of the DNA linear rod, the DNA tetrahedron, and the T4 bacteriophage without imposing symmetry constraints (SI Appendix, Fig. S17). These successful reconstructions show that our method is able to reconstruct complex shapes even in the absence of symmetry constraints. Next, we simulated SMLM experiments of intrinsically asymmetric structures (spiral and duckling, Figs. 4A-B, D-E, and SI Appendix, Fig. S18) and applied our method to reconstruct them. Again, we were able to successfully reconstruct complex asymmetric 3D shapes with excellent resolutions and fidelities (Figs. 4C,F, and SI Appendix, Fig. S19). All in all, we conclude that the method can be applied to asymmetric shapes and that symmetry considerations are not necessary to retrieve the original structure.

Discussion

Recently, single-particle averaging methods used 3D single-molecule localization images to reveal the 3D structures of several biological objects, such as the nuclear pore complex (8), the ESCRT machinery at HIV assembly sites (6), and the centrosome machinery (9). These objects were highly symmetrical (cylindrical or spherical) and the previous approaches used relied on the use of templates, making it difficult to apply similar methodologies to more complex biological objects or to unknown structures. More recently, it was shown that 3D single-molecule localization data can be directly used to reconstruct a 3D shape (20), making it a valuable approach when raw 3D localizations are available. This method, however, requires a template structure to detect and align single particle images and does not explicitly deal with sample heterogeneity or particle symmetry.

Here, we present a method that is able to reconstruct the 3D structures of well-characterized DNA origami and protein complexes with 3D isotropic resolutions. Our results demonstrate that conventional single-particle reconstruction algorithms can be adapted to solve several issues inherent to super-resolution microscopies, despite recent reports (20). First, we were able to automatically discard particles that were not efficiently labeled, displayed structural inhomogeneities due to the fabrication process, or to the immobilization conditions. Second, the ability to obtain different projections from the particles allowed us to reach isotropic 3D resolutions, with high resolutions in all directions. Third, the reconstruction method did not rely on *a priori* information about the structure, which minimized template dependence. We note, however, that knowledge of the particle symmetry was important to converge faster to accurate reconstructions. Finally, the resolution of the reconstruction far outstripped the resolution of the individual particles lacking labeling sampling, highlighting the ability of the method to further surpass the Nyquist resolutions attainable by direct super-resolution methods.

Reference-free cross-correlation based alignment and classification methods with MRA/MSA tend to perform poorly for datasets with low signal to noise ratios (SNR). However, SMLM data sets are highly contrasted due to the relatively good SNR of each detected single fluorescent molecule with respect to the background noise. In fact, our simulations of various densities of contaminating localizations in conjunction with reduced specific labeling densities showed that reference-free cross-correlation based alignment and classification methods are very robust to noise in SMLM datasets. It is also worth noting that the depth of field in single-molecule localization microscopy is typically 300–800 nm, depending on the emission intensity of the fluorophore (21–23). Thus, imaging of objects larger than the depth of field will require the acquisition and averaging of images at different axial positions to obtain projection images containing information from the whole particle volume.

A correct angular reconstitution requires an even distribution of single particles with random orientations on the support onto which the specimen is adsorbed so that all views are well represented. However, as observed in the field of EM SPR, the angular distribution of projections may be uneven due physical effects, such as interactions with the support, or to the specific cellular distribution of the complex under study. Under these conditions, an angular imbalance of projections can result in an anisotropic resolution and distortions (e.g. stretching) of the structure (24, 25). To overcome this problem, iterative image processing procedures to retrieve rare views have been developed in the EM SPR community (26), and can be adapted to SMLM-based imaging. After an iterative procedure of image processing and a collection of substantially larger data sets, rare views are brought to statistical significance in order to achieve reliable isotropic reconstructions. This method has been widely used and may be future directions of this work (27–30). Similarly to approaches taken in the EM SPR community (31–33), exploration of different support chemistries will help prevent any preferred orientations during image acquisition.

In addition to imaging DNA origami nanostructures, our method is directly applicable to protein assemblies labeled by genetic fusions, antibodies, exchange-PAINT (34). By employing iPANT (35) as a generic imaging method, our approach should allow for the exploration of 3D isotropic supramolecular structures in other fields, such as nanotechnology, colloid science, interface science and soft matter physics. The ability of our method to reconstruct structures labeled with extremely low labeling densities could alleviate many problems such as low photoactivation efficiency, probe accessibility, and steric hindrance. Excitingly, the combination of our approach with multi-color acquisition could be used in future to retrieve the 3D structures of supramolecular complexes in their natural environments at unsurpassed resolutions.

Materials and Methods

Design and assembly of DNA origami structures

DNA origami nanostructures were designed using the honeycomb-lattice version of the caDNAno software (<http://cadnano.org/>). Assembly of DNA nanostructures was accomplished in a one-pot reaction by mixing scaffold strands derived from M13 bacteriophage at 20 nM with 200 nM of each oligonucleotide staple strand in a folding buffer

containing 5 mM Tris, 1 mM EDTA, pH 8, and a concentration of MgCl₂ adjusted for each nanostructure. MgCl₂ conditions listed in parenthesis: linear-rod origami (18 mM), tetrahedron (12 mM). The strand mixture was then annealed in a PCR thermal cycler using a fast linear cooling step from 80°C to 65°C over 1 hour, then 42 hours linear cooling ramp from 64°C to 24°C.

Agarose gel electrophoresis

Annealed samples were subjected to gel electrophoresis in 1% TBE buffer including 11 mM MgCl₂, at 70V for 3 hours in an ice-water bath. Gels were stained with SyberR Safe before imaging. Bands corresponding to the correctly folded structures were then visualized with ultraviolet light and cut out from the gel. Excised bands were crushed and transferred into DNA gel extraction spin column (BIO-RAD, Catalog number: 732-6166). The DNA structure solution was recovered by centrifugation of the loaded column for 10 minutes at 10,000 g.

TEM imaging

For imaging, 2.5 µL of annealed sample was adsorbed for 2 minutes onto glow-discharged, carbon-coated TEM grids. The grids were then stained for 60 seconds using a 2% aqueous uranyl formate solution containing 25 mM NaOH. Imaging was performed at 80 keV.

Imager strands for DNA-PAINT imaging

Atto647n/Alexa488 imager strand sequence : 5'-TATGTAGATC-3' Dye (Eurogentec, France). Sequence of biotin-oligo: 5'-GAATCGGTACAGTACAACCG-3' biotin (Eurogentec, France).

Microfluidics channel functionalization

Linear rods were immobilized by using specific biotin/neutravidin interactions. Biotin-silane-PEG/Silane-PEG/neutravidin coating was performed in several steps: (1) the glass coverslip surface of the microfluidics channels was activated by incubating in a solution of KOH (1M for 20 minutes) and then rinsed by flushing a solution of borate potassium buffer (2) 5 µl of Biotin-silane-PEG (20 mg of Biotin-silane-PEG (Laysan Bio) diluted in 220 µl of methanol) were mixed with 150 µl of silane-PEG (10 mg of silane-PEG (Laysan Bio) diluted in 200 µl of borate potassium buffer) and were injected into microfluidics channels; (3) channels were incubated overnight; (4) channels were rinsed several times with ddH₂O; (5) a 1 mg/ml solution of neutravidin in PBS was injected and incubated for 30'; (6) channel was extensively rinsed with ddH₂O. Tetrahedrons were immobilized onto poly-L-Lysine coated microfluidics channels. Channels were then filled with a solution of 0.01 % (v/v) of

poly-L-Lysine, incubated for 20' and rinsed several times with ddH₂O.

Setup for super-resolution experiments

Super-resolution imaging was carried out on a custom-built PALM microscope, using objective-type total internal reflection fluorescence (TIRF). Two laser lines were used for excitation: 488 nm (OBIS, LX 488-50, Coherent Inc.) and 640 nm (OBIS, LX 640-100, Coherent Inc.) depending on the fluorophore being excited. Laser beams were expanded, passed through an acousto-optic tunable filter (AOTFnC-400.650-TN, AA opto-electronics) and coupled into the back focal plane of an oil-immersion objective (Plan-Apochromat, 100x, 1.4NA oil DIC, Zeiss) using achromatic lenses. A multi-band dichroic mirror (zt405/488/561/638rpc, Chroma) was used to decouple excitation and emission. Fluorescence signal was spectrally filtered by emission filters (ET525/50m and ET700/75m, Chroma Technology) and imaged on an electron-multiplying charge-coupled device (EMCCD) camera (iXon X3 DU-897, Andor Technologies). A 1.5x telescope was used in the emission path to obtain a final imaging magnification of ~150 fold, corresponding to a pixel size of 105 nm. Acquisition software controlling lasers, filter wheels, and camera were homemade using LabView 2010 (National Instruments, France). For more details see Cattoni *et al.*(36).

DNA-PAINT imaging

Experiments were performed in a custom-made PDMS microfluidics flow chamber (see Fig. S5). Surface functionalization is described above. Origami were flushed into a channel of the chamber (inner volume capacity of ~5 µl) at a concentration of 250 pM and incubated for 30 min. Next, 100 nm TetraSpeck beads (Invitrogen, France) were flushed into the chamber and used as fiducial marks for drift correction. Finally, imager strands (oligo-Alexa488, for linear rod and oligo-Atto647n for tetrahedron) were diluted to a final concentration of 5 nM in imaging buffer (Tris-HCl pH 8, 10 mM MgCl₂, 1 mM EDTA, 0.05% Tween 20 (34)) and injected into the channel.

Camera gain was fixed at 200. Movies (typically 15000-20000 frames) were recorded at a rate of 5 Hz in frame-transfer mode with ~50 mW of continuous laser illumination (488 nm laser for linear rod, and 642 nm for tetrahedron).

Single fluorophore localization, drift correction and image reconstruction

Image processing was performed using Matlab 2011 (The Mathworks, Inc). Single molecule localizations and fiducial marks were detected using MTT- analysis (37). A minimum intensity threshold was applied to filter localizations derived from background noise. Drift correction was assessed using vPALM, a custom-made software where fiducial marks trajectories were extracted (for more details refer to Fiche *et al.* (38)). Experiments with a drift correction precision larger than 20 nm were discarded.

Further analysis of single-molecule localizations was performed with several custom-made algorithms. Localizations were plotted in a single-image (pointillist representation), and drift corrected. Drift correction involved the following steps: (1) for each

field of view, the trajectories of at least four fiducial marks were chosen and the mean trajectory was calculated by averaging their trajectories; (2) The quality of the drift correction was estimated by subtracting the mean trajectory to all the trajectories and calculating the standard deviations along x and y for the beads used for correction; (3) when the standard deviation of the corrected trajectories was acceptable (<10nm), the coordinates of the localizations corresponding to DNA-PAINT events were corrected by using the mean trajectory. Otherwise, the experiment was discarded.

Drift-corrected localizations were then sorted into clusters using an algorithm described elsewhere (36). For each cluster, the main axes were determined by using eigenvector decomposition. Clusters were aligned to match the major axis with the x-direction and the minor axis with the y-direction. Cluster dimensions were measured as follows: length was defined as the maximum distance between localizations along the x-axis, while width was calculated from the FWHM of the distribution of localizations along the y-coordinate. Clusters with less than a minimum number of localizations (100 for linear rod and 50 for tetrahedron) were discarded to eliminate imager strands bound non-specifically to the surface. For linear rods, only clusters with a length >25 nm and <250 nm, and a maximum width of 100 nm were considered to avoid single imager strands or large aggregates of origami. For tetrahedron, only clusters with dimensions >25 nm and <200 nm were considered. Clusters passing this minimal criterium were converted into probability density images using a super-resolution pixel size of 2.2 nm for linear rod and 3.3 nm for tetrahedron (36).

Localization coordinates and uncertainties were used to estimate the probability distribution of localization for each single emitter. Probability density images were thus obtained by superimposing the contributions of all the detected localizations after drift correction (39–42). This probability density is the most commonly used approach to representing the underlying structure as it provides the probability of having a fluorescent molecule at a given position.

Particle averaging analysis and 3D reconstruction

Particle averaging analysis was implemented using IMAGIC (43) (Image Science Software, GmbH, Germany). This choice was made because IMAGIC allows access to modify the scripts used for each step in the process, which was critical to find the most optimal procedure for particle classification and reconstruction from SMLM data. Most operations can be implemented on other EM software packages (see extensive list in <http://www.emdatabank.org/emsoftware.html>). Initial data sets of images were obtained from a stack of individual probability density images derived from single-molecule localization analysis. The probability density of localization from each selected cluster (particle) was represented as a 100×100 pixels image in TIFF format. These images were converted to MRC format using ImageJ (44). Final image stacks had 5427 particles for linear rods, 2219 particles for tetrahedrons, and 4000 particles for simulated structures. We ensured that these number of raw particles produced robust reconstructions by evaluating the FSC between two independent reconstructions derived from half the total number of particles (see main text). Subsequently, particles were band-pass filtered, aligned and classified using Multivariate Statistical Analysis (MSA) classification (15). For unbiased reconstructions (without initial model), selected references from these classes (based on the visual match between the

class average and the individual particles) were further utilised to perform multi-reference alignment (MRA) of the images. To perform biased reconstructions (with initial model) a set of 2-D forward projection images with known Euler angles were implemented as references (“anchor set”). After three cycles of MRA/MSA, final class averages were obtained (200 and 250 classes for linear rod and tetrahedron, respectively) for the unbiased reconstruction, and 250 and 400 for the biased reconstructions.

References (best projections) derived from the final class averages were selected to apply angular reconstitution. For the linear rod, 12 (unbiased) and 15 (biased) references were selected. For the tetrahedron, 29 (unbiased) and 55 (biased) references were employed. C2 and C6 symmetries were applied for 3D reconstructions of origami and bacteriophage simulations reconstructions, respectively. For unbiased template-free reconstructions, 3D reconstructions were back-projected with different angles to serve as references (“anchor set”) for further iterative refinement cycles of reconstructions. Template-free reconstructions were performed with a single model generation iteration. Note that the quality of the final 3D reconstructions could be further improved by using models of increasing quality to obtain classes. This analysis scheme allowed for the characterization of sample heterogeneity, including different orientations of the same species (i.e. projections) or different species.

Fourier Ring and Shell Correlations

The resolution of 3D reconstructions was evaluated by Fourier Shell Correlation (43, 45, 46). The initial set of single-particles was divided into two independent groups each containing half the particles (chosen randomly). 3D reconstructions were computed for each independent group of single-particles. The resolution was assigned from the FSC curve by estimating the point where the FSC crosses a threshold of 0.143 (18) and is similar to that employed for super-resolution imaging using the Fourier Ring Correlation (19).

To validate our 3D reconstructions we additionally computed their FSC against their respective models. FSCs between theoretical high-resolution models and 3D reconstructions were calculated using freely accessible software provided by the Protein Data Bank (<https://www.ebi.ac.uk/pdbe/emdb/validation/fsc>).

Fourier Ring Correlation (FRC) of localizations obtained for single linear rods and Tetrahedron origamis using DNA-PAINT was performed in Matlab using routines developed in (19). Each origami cluster time-series was divided into blocks of 100 to 1000 frames and assigned randomly to two distinct half sets to compute the Fourier Ring Correlation. The operation was performed five times and averaged for 100 random origamis structures to get a resulting mean resolution value.

Simulations of DNA PAINT datasets

The effect of labeling spacing on the robustness of the single-particle reconstruction method was tested using computer simulations. A high-resolution theoretical model of the T4 bacteriophage was produced at 5 nm resolution. From this model, we designed a series of simulated docking strands spanning the whole structure at a minimum distance of 5 nm. To

generate a simulated DNA PAINT model, we sequentially and randomly chose docking strands in the model and populated them with an average of 15 localizations. An iterative process ensured that the distance between the selected docking strands was not smaller than the labeling spacing being simulated. This process was repeated for each DNA PAINT model until no more docking strands satisfying these conditions were available. 3D DNA PAINT models were converted into 2D projected densities as described above generating the raw particles. For each labeling spacing, 4000 single particles were generated and used to obtain a 3D reconstruction as described above. In case noise was considered in the simulation, additional nonspecific binding sites were randomly added within a 150 nm radius of each structure center and populated with an average of 15 localizations (similar to specific sites). Number of nonspecific binding sites was chosen as a percentage of the total number of specific binding sites used to label the structure.

The same procedure was applied to the spiral and duckling structures (with a labeling spacing and a localisation precision of 6 nm and 15 nm for the spiral and of 5 nm and 10 nm for the duckling) to validate our approach with asymmetric structures.

Software and scripts

MATLAB m-files and IMAGIC scripts are accessible at Github under project name 3DreconstructionSMLM (<https://github.com/marcnol/3DreconstructionSMLM>).

Acknowledgements

Research was supported by a European Research Council Starting Grant to M.N. (ERC-Stg-260787), the French National Research Agency to G.B. (ANR-16-CE09-0004-01 and ANR-15-CE09-0003-02), and a BME startup fund to Y.K. D.S. is the recipient of a scholarship from CONICYT PAI/INDUSTRIA 79090016. We acknowledge support from France-BioImaging (FBI, ANR-10-INSB-04).

References

1. Low HH, et al. (2014) Structure of a type IV secretion system. *Nature* 508(7497):550–553.
2. Schmidt C, et al. (2016) The cryo-EM structure of a ribosome-Ski2-Ski3-Ski8 helicase complex. *Science* 354(6318):1431–1433.
3. Frank J (2017) Advances in the field of single-particle cryo-electron microscopy over the last decade. *Nat Protoc* 12(2):209–212.
4. Schermelleh L, Heintzmann R, Leonhardt H (2010) A guide to super-resolution fluorescence microscopy. *J Cell Biol* 190(2):165–175.
5. Shtengel G, et al. (2009) Interferometric fluorescent super-resolution microscopy resolves 3D cellular ultrastructure. *Proc Natl Acad Sci U S A* 106(9):3125–3130.
6. Van Engelenburg SB, et al. (2014) Distribution of ESCRT machinery at HIV assembly sites reveals virus scaffolding of ESCRT subunits. *Science* 343(6171):653–656.
7. Schermelleh L, et al. (2008) Subdiffraction multicolor imaging of the nuclear periphery with 3D structured illumination microscopy. *Science* 320(5881):1332–1336.
8. Szymborska A, et al. (2013) Nuclear pore scaffold structure analyzed by super-resolution microscopy and particle averaging. *Science* 341(6146):655–658.
9. Mennella V, et al. (2012) Subdiffraction-resolution fluorescence microscopy reveals a domain of the centrosome critical for pericentriolar material organization. *Nat Cell Biol* 14(11):1159–1168.
10. Sauer M, Heilemann M (2017) Single-Molecule Localization Microscopy in Eukaryotes. *Chem Rev* 117(11):7478–7509.
11. Rothenmund PWK (2006) Folding DNA to create nanoscale shapes and patterns. *Nature* 440(7082):297–302.
12. Douglas SM, et al. (2009) Self-assembly of DNA into nanoscale three-dimensional shapes. *Nature* 459(7245):414–418.
13. Schmied JJ, et al. (2012) Fluorescence and super-resolution standards based on DNA origami. *Nat Methods* 9(12):1133–1134.
14. Iinuma R, et al. (2014) Polyhedra self-assembled from DNA tripods and characterized with 3D DNA-PAINT. *Science* 344(6179):65–69.
15. Heel M van, Portugal RV, Schatz M (2016) Multivariate Statistical Analysis of Large Datasets: Single Particle Electron Microscopy. *OJS* 06(04):701–739.
16. Van Heel M (1987) Angular reconstitution: a posteriori assignment of projection directions for 3D reconstruction. *Ultramicroscopy* 21(2):111–123.
17. Harauz G, van Heel M (1986) Exact filters for general geometry three dimensional reconstruction. *Optik* 73(4):146–156.

18. Rosenthal PB, Henderson R (2003) Optimal determination of particle orientation, absolute hand, and contrast loss in single-particle electron cryomicroscopy. *J Mol Biol* 333(4):721–745.
19. Nieuwenhuizen RPJ, et al. (2013) Measuring image resolution in optical nanoscopy. *Nat Methods* 10(6):557–562.
20. Broeken J, et al. (2015) Resolution improvement by 3D particle averaging in localization microscopy. *Methods and applications in fluorescence* 3(1):014003.
21. Izeddin I, et al. (2012) PSF shaping using adaptive optics for three-dimensional single-molecule super-resolution imaging and tracking. *Opt Express* 20(5):4957–4967.
22. Oudjedi L, et al. (2016) Astigmatic multifocus microscopy enables deep 3D super-resolved imaging. *Biomed Opt Express* 7(6):2163–2173.
23. Huang B, Wang W, Bates M, Zhuang X (2008) Three-dimensional super-resolution imaging by stochastic optical reconstruction microscopy. *Science* 319(5864):810–813.
24. Sorzano CO, et al. (2001) The effect of overabundant projection directions on 3D reconstruction algorithms. *J Struct Biol* 133(2-3):108–118.
25. Boisset N, et al. (1998) Overabundant single-particle electron microscope views induce a three-dimensional reconstruction artifact. *Ultramicroscopy* 74(4):201–207.
26. Schatz M, Orlova EV, Dube P, Jäger J, van Heel M (1995) Structure of *Lumbricus terrestris* hemoglobin at 30 Å resolution determined using angular reconstitution. *J Struct Biol* 114(1):28–40.
27. Serysheva II, Schatz M, van Heel M, Chiu W, Hamilton SL (1999) Structure of the skeletal muscle calcium release channel activated with Ca²⁺ and AMP-PCP. *Biophys J* 77(4):1936–1944.
28. Baker MR, Fan G, Serysheva II (2015) Single-Particle Cryo-EM of the Ryanodine Receptor Channel in an Aqueous Environment. *Eur J Transl Myol* 25(1):4803.
29. Stark H, et al. (1997) Visualization of elongation factor Tu on the *Escherichia coli* ribosome. *Nature* 389(6649):403–406.
30. Stark H, et al. (1995) The 70S *Escherichia coli* ribosome at 23 Å resolution: fitting the ribosomal RNA. *Structure* 3(8):815–821.
31. Vinothkumar KR, Henderson R (2016) Single particle electron cryomicroscopy: trends, issues and future perspective. *Q Rev Biophys* 49:e13.
32. Cheng Y, Grigorieff N, Penczek PA, Walz T (2015) A primer to single-particle cryo-electron microscopy. *Cell* 161(3):438–449.
33. Thompson RF, Walker M, Siebert CA, Muench SP, Ranson NA (2016) An introduction to sample preparation and imaging by cryo-electron microscopy for structural biology. *Methods* 100:3–15.
34. Jungmann R, et al. (2014) Multiplexed 3D cellular super-resolution imaging with DNA-PAINT and Exchange-PAINT. *Nat Methods* 11(3):313–318.

35. Aloi A, Vilanova N, Albertazzi L, Voets IK (2016) iPAINT: a general approach tailored to image the topology of interfaces with nanometer resolution. *Nanoscale* 8(16):8712–8716.
36. Cattoni DI, Fiche J-B, Valeri A, Mignot T, Nollmann M (2013) Super-resolution imaging of bacteria in a microfluidics device. *PLoS One* 8(10):e76268.
37. Serge A, Bertaux N, Rigneault H, Marguet D (2008) Dynamic multiple-target tracing to probe spatiotemporal cartography of cell membranes. *Nat Methods* 5(8):687–694.
38. Fiche J-B, et al. (2013) Recruitment, assembly, and molecular architecture of the SpolIIIE DNA pump revealed by superresolution microscopy. *PLoS Biol* 11(5):e1001557.
39. Betzig E, et al. (2006) Imaging intracellular fluorescent proteins at nanometer resolution. *Science* 313(5793):1642–1645.
40. Bates M, Huang B, Dempsey GT, Zhuang X (2007) Multicolor super-resolution imaging with photo-switchable fluorescent probes. *Science* 317(5845):1749–1753.
41. York AG, Ghitani A, Vaziri A, Davidson MW, Shroff H (2011) Confined activation and subdiffractive localization enables whole-cell PALM with genetically expressed probes. *Nat Methods* 8(4):327–333.
42. Wolter S, et al. (2012) rapidSTORM: accurate, fast open-source software for localization microscopy. *Nat Methods* 9(11):1040–1041.
43. van Heel M, Harauz G, Orlova EV, Schmidt R, Schatz M (1996) A new generation of the IMAGIC image processing system. *J Struct Biol* 116(1):17–24.
44. Schneider CA, Rasband WS, Eliceiri KW (2012) NIH Image to ImageJ: 25 years of image analysis. *Nat Methods* 9(7):671–675.
45. Saxton WO, Baumeister W (1982) The correlation averaging of a regularly arranged bacterial cell envelope protein. *J Microsc* 127(Pt 2):127–138.
46. Unser M, Trus BL, Steven AC (1987) A new resolution criterion based on spectral signal-to-noise ratios. *Ultramicroscopy* 23(1):39–51.

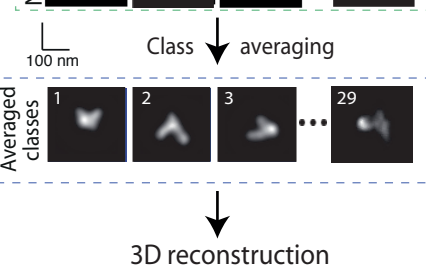
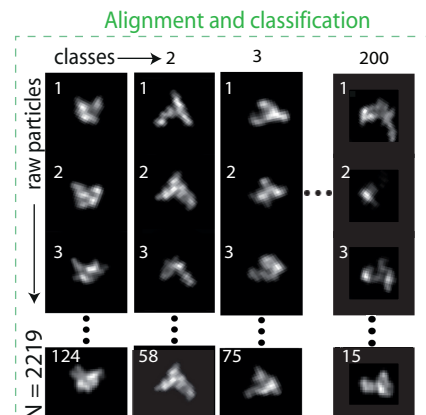
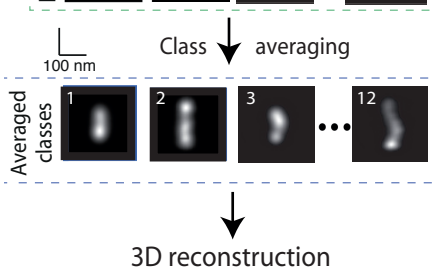
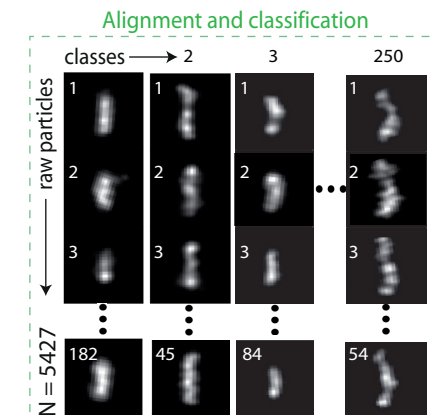
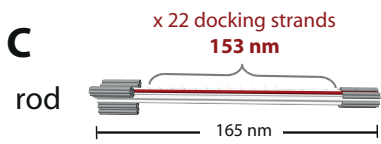
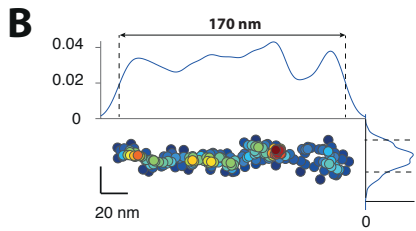
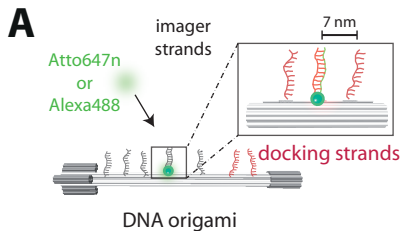
Figure legends

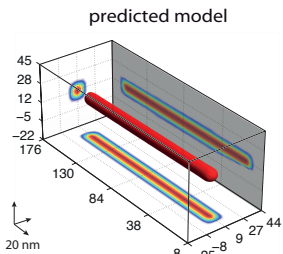
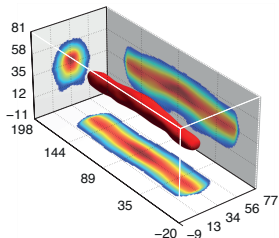
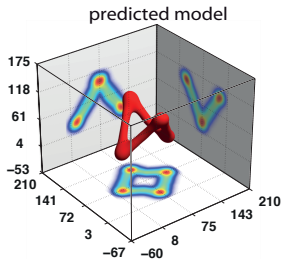
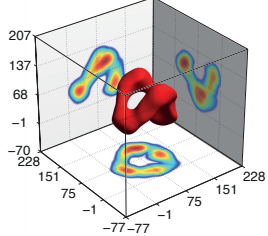
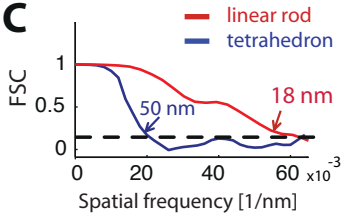
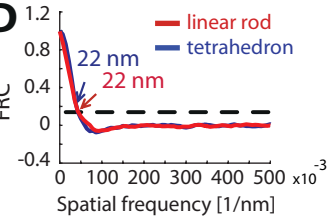
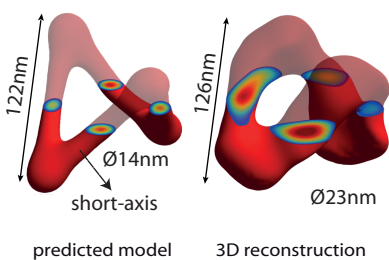
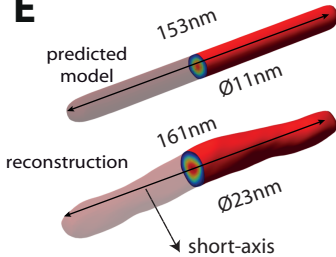
Fig. 1. Self-assembly of DNA origami and single-particle averaging. (A) Schematic representation of DNA origami and DNA PAINT strategy. Docking strands were positioned on the surface of the origami at regular spacings, imager strands were localized with nanometer precision. (B) Single, surface-bound DNA origami can be visualized by DNA PAINT (left and right images). The typical profile width was 14 nm (bottom panel). (C-D) Top panels: schematic representations of linear rod and tetrahedron. Bottom panels: raw particles were reoriented and retranslated, aligned and classified to obtain class averages. Total number of raw particles from over 20 independent experiments: 5427 for linear rod and 2219 for tetrahedron.

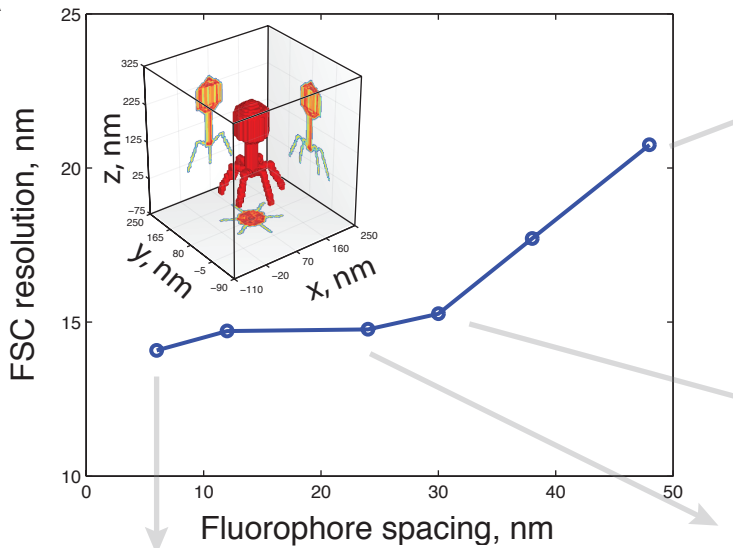
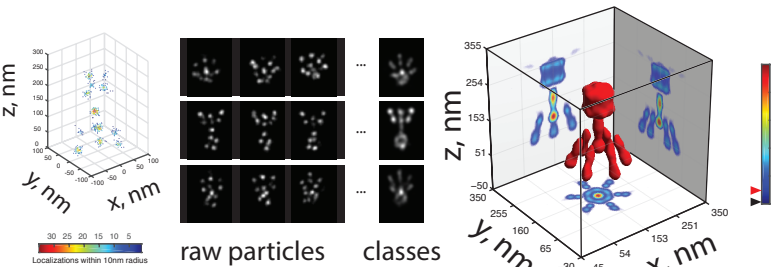
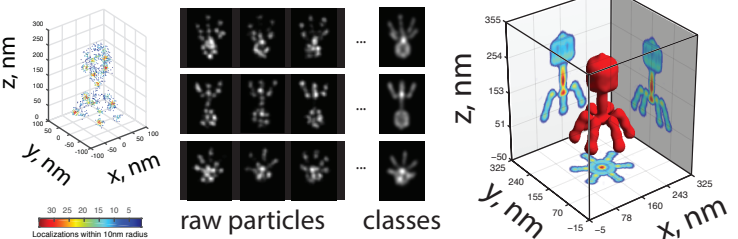
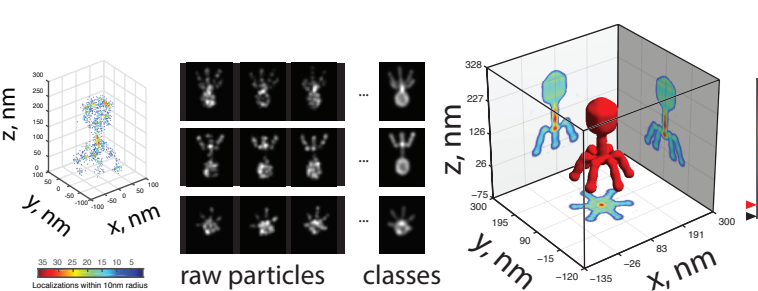
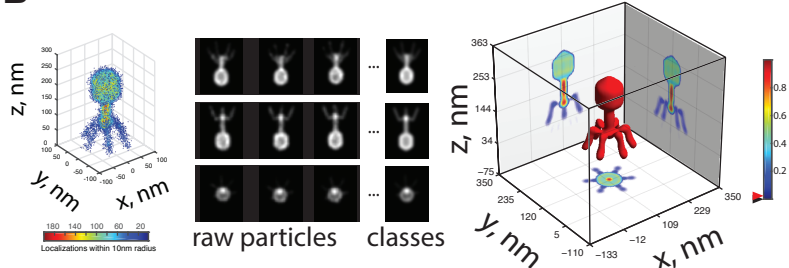
Fig. 2. 3D structures of DNA origami by single-particle reconstruction. (A-B) Left panels: 3D structures of linear rod and tetrahedron from theoretical models. Right panels: template-free 3D reconstructions. Black and red triangles on colormaps represent the threshold and iso values used for the intensity projections and 3D representation of the structures, respectively. (C) Fourier shell correlation of the final 3D reconstructions. (D) Average Fourier ring correlation obtained by averaging the FRC curves of 100 single particles for the linear rod and the tetrahedron. (E) Direct comparison of the reference model and 3D reconstructions.

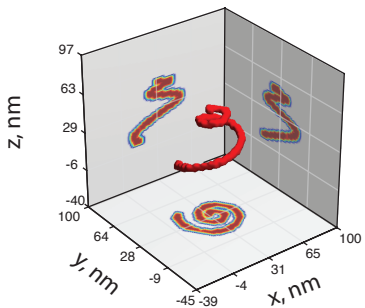
Fig. 3. Fidelity of 3D single-particle reconstructions for different labeling spacings. (A) Robustness of the 3D single-particle reconstruction as a function of labeling spacing measured as the FSC resolution obtained by correlating the high-resolution theoretical model and the 3D reconstruction. Inset: 3D structure of the high-resolution model of the T4 bacteriophage (250 nm in height, 150 nm in diameter). (B-E) Reconstruction results for different labeling spacings. Left panel: 3D representation of single-molecule localizations from a single simulated particle. Middle panels: projections of raw particles and class averages. Right panel: final 3D single-particle analysis reconstruction. 4000 raw particles were used for each labeling spacing. Black and red triangles on colormaps represent the threshold and iso values used for the intensity projections and 3D representation of the structures, respectively.

Fig. 4. 3D reconstructions of asymmetric structures. (A-D) High-resolution structural models of a spiral-shape and a duckling-shape structure. (B-E) Class averages produced by cumulating similar projections of the spiral-shape and duckling structures generated with a 6 and 5 nm labeling spacing, respectively. (C-F) 3D reconstructions of the spiral and duckling structures. Black and red triangles on colormaps represent the threshold and iso values used for the intensity projections and 3D representation of the structures, respectively.



A**3D reconstruction****B****3D reconstruction****C****D****E**

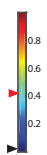
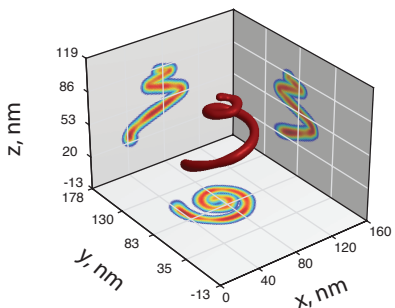
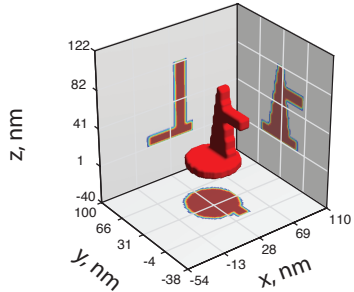
A**E****D****C****B**

A**Model****B**

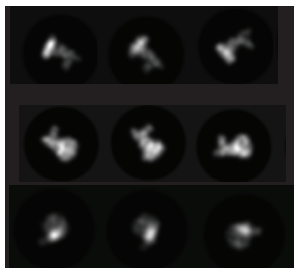
raw particles



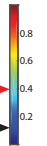
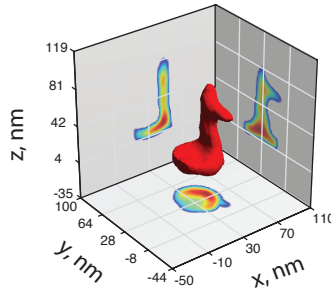
classes

C**3D reconstruction****D****Model****E**

raw particles



classes

F**3D reconstruction**

SI Appendix

Template-free reconstruction of nanomolecular structures from nanoscopy images with isotropic 3D resolution

Desirée Salas, Antoine Le Gall, Jean-Bernard Fiche, Alessandro Valeri, Yonggang Ke, Patrick Bron, Gaetan Bellot, Marcelo Nollmann

FIGURE S1 : STRAND DIAGRAMS FOR LINEAR ROD.

FIGURE S2. SELF-ASSEMBLY OF LINEAR ROD.

FIGURE S3. STRAND DIAGRAMS FOR TETRAHEDRON.

FIGURE S4. SELF-ASSEMBLY FOR TETRAHEDRON.

FIGURE S5. DNA-PAINT IMAGING OF DNA ORIGAMI IN MICROFLUIDICS CHAMBER

FIGURE S6. DNA-PAINT IMAGING OF LINEAR ROD

FIGURE S7. FLOWCHART OF FULL IMAGE PROCESSING

FIGURE S8. FLOWCHART OF THE GENERAL PROCESS OF SINGLE PARTICLE ANALYSIS (2D) AND RECONSTRUCTION PROCESS (3D)

FIGURE S9. EXAMPLE OF PARTICLE AVERAGING METHOD IN DIFFERENT STEPS

FIGURE S10. SELECTED REFERENCES AND UNBIASED AND BIASED 3D RECONSTRUCTION

FIGURE S11. CHARACTERIZATION OF 3D RECONSTRUCTION WITH A REFERENCE (BIASED - RECONSTRUCTION)

FIGURE S12. Fourier Ring Correlation of DNA-PAINT localization data

FIGURE S13. VALIDATION OF SINGLE-PARTICLE RECONSTRUCTION BY SIMULATIONS

FIGURE S14. FOURIER SHELL CORRELATION OF BACTERIOPHAGE T4 RECONSTRUCTIONS FOR VARIOUS LABELING DENSITIES

FIGURE S15. BACTERIOPHAGE T4 RECONSTRUCTIONS WITH AND WITHOUT MODEL

FIGURE S16. CLASS AVERAGES OF T4 SIMULATIONS AT VARIOUS LABELING DENSITIES WITH INCREASING NOISE CONTAMINATION LEVELS.

FIGURE S17. LINEAR ROD, TETRAHEDRON and BACTERIOPHAGE T4 RECONSTRUCTIONS WITHOUT SYMMETRY CONSTRAINTS

FIGURE S18. EXAMPLES OF EIGEN IMAGES OF THE DIFFERENT STRUCTURES STUDIED IN THIS WORK.

FIGURE S19. FSC AND EULER ANGLE DISTRIBUTIONS OF 3D RECONSTRUCTIONS OF ASYMMETRIC STRUCTURES

SUPPLEMENTARY TABLE 1. SEQUENCES OF LINEAR ROD STAPLES AND DOCKING STRANDS.

SUPPLEMENTARY TABLE 2. SEQUENCES OF TETRAHEDRON STAPLES AND DNA-PAINT DOCKING STRANDS.

REFERENCES

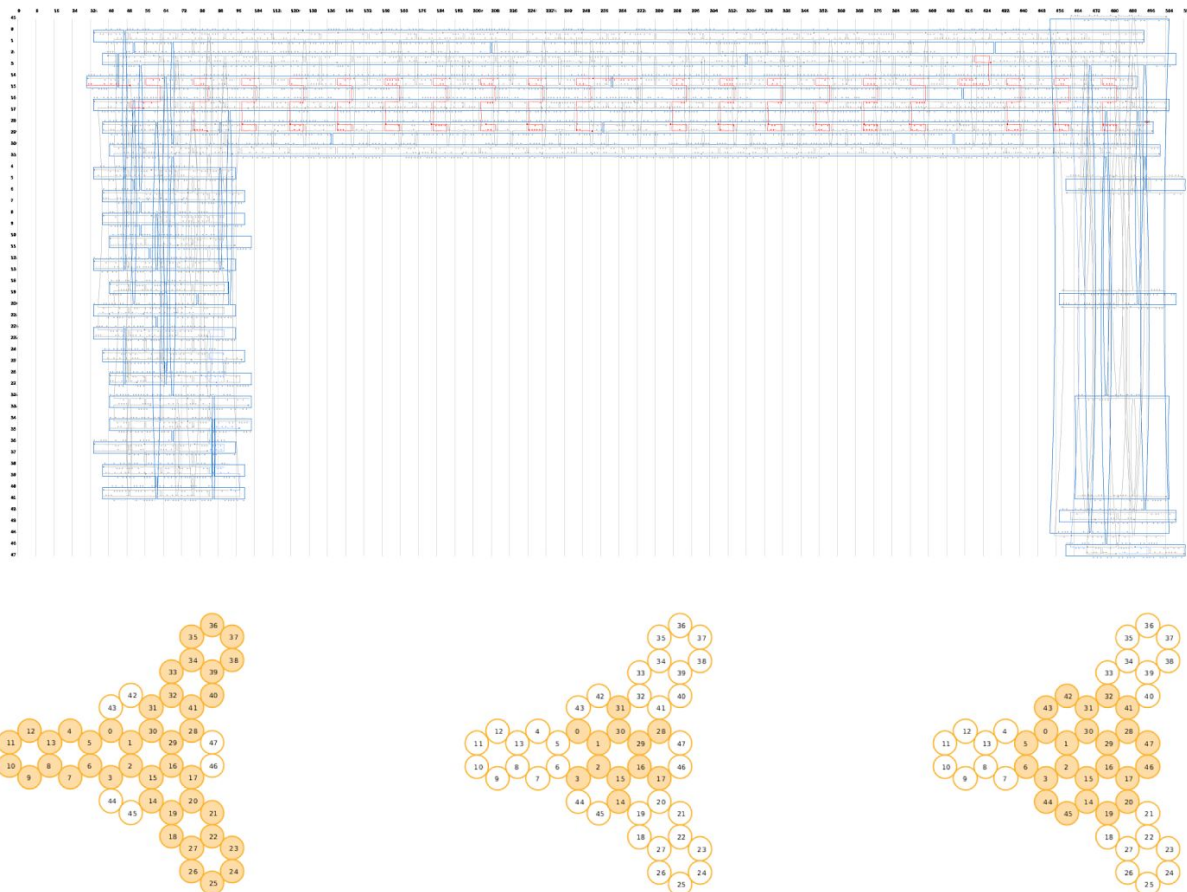


FIGURE S1 : STRAND DIAGRAMS FOR LINEAR ROD.

Schematic design of the linear rod DNA origami. Blue lines represent the p8064 single-stranded DNA scaffold. Grey lines represent core staple strands. Red lines represent DNA-PAINT docking sites. Light blue represents biotin docking strands. Arrows indicate 3'-ends of DNA. Schematic representations of the profile of the structure are shown in the left as a collection of yellow circles. Assembly and characterization of linear rods are presented in Figure S2.

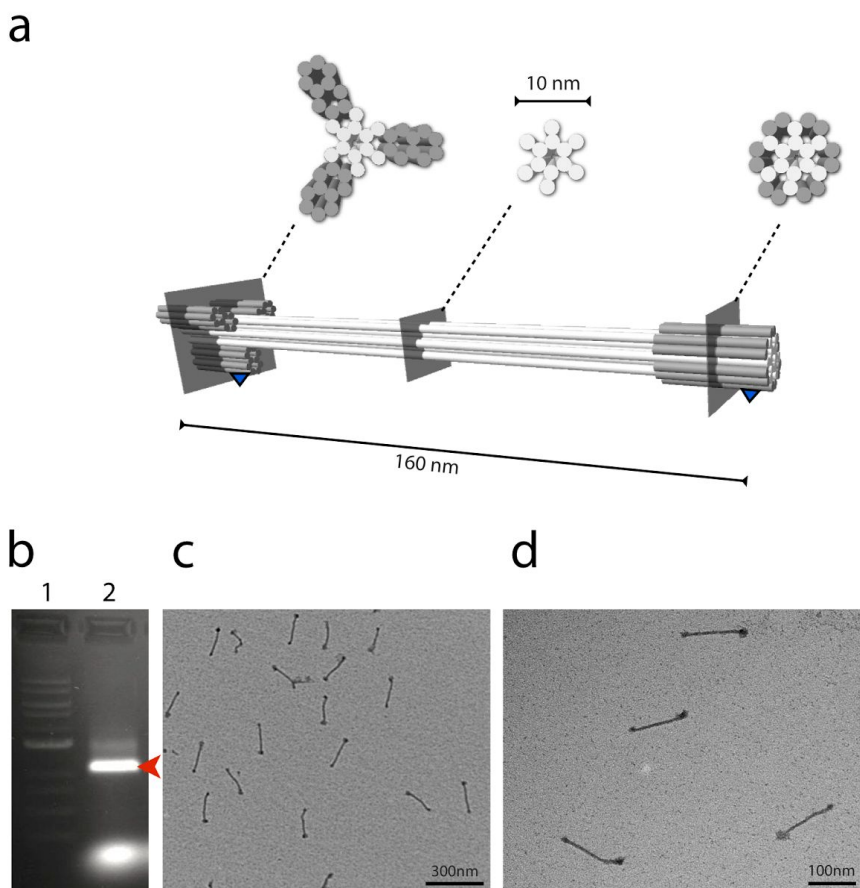


FIGURE S2. SELF-ASSEMBLY OF LINEAR ROD.

(a) Three-dimensional cartoon view of the rod DNA origami, 165 nm-long 12-helix bundle. And, illustration of the intersections of the linear rod design. In blue, biotinylated strands immobilize the structures to glass surfaces for fluorescence imaging. (b) Gel electrophoresis of the linear rod. Gel lane 1 is a 1-kb ladder. Gel lane 2 is the assembly reaction. Gel band corresponding to desired product is marked with red arrowhead. Gel electrophoresis was performed using 1.5 % native agarose gel. (c,d) Typical transmission electron microscopy (TEM) images of the linear rod are shown.

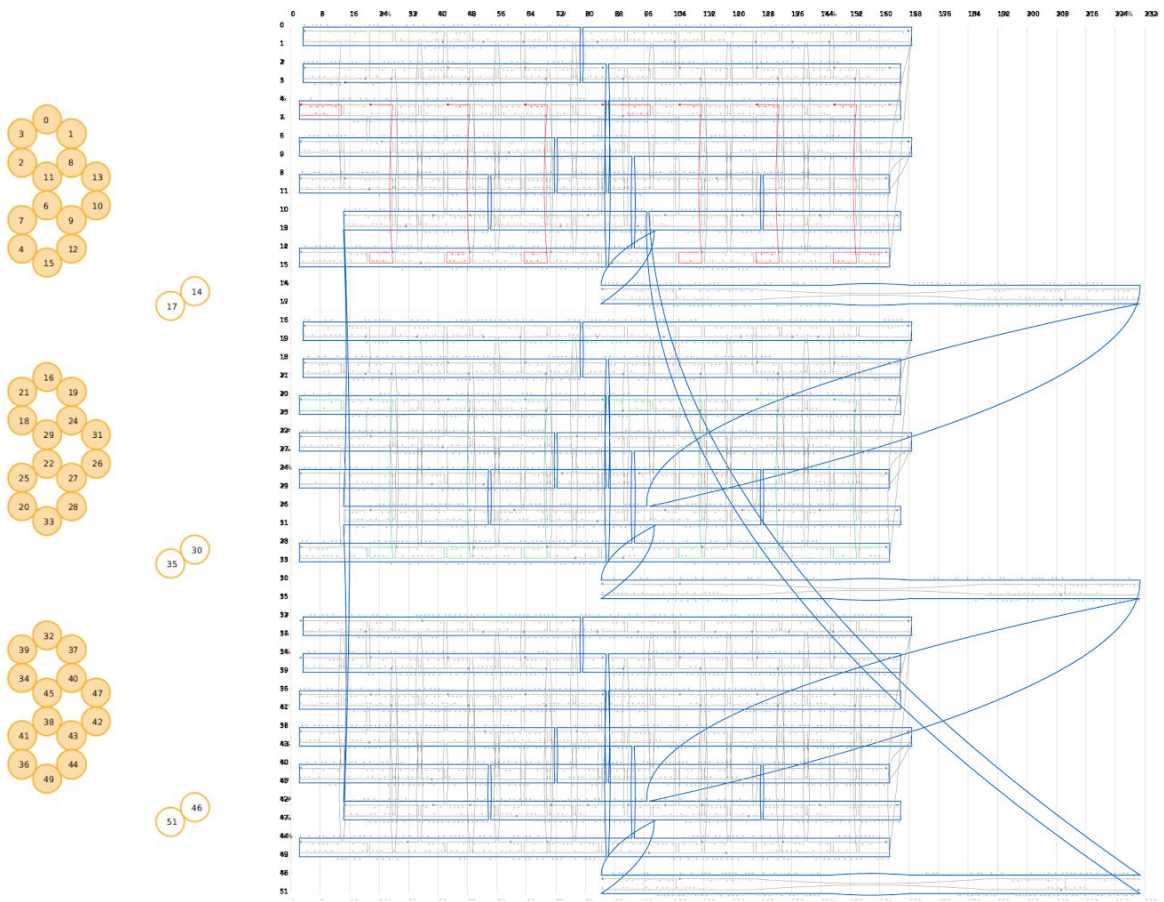


FIGURE S3. STRAND DIAGRAMS FOR TETRAHEDRON.

The strand in blue is the p7060 scaffold strand. Grey lines represent core staple strands. In red, DNA-PAINT docking sites from 'arm X'. In green, DNA-PAINT docking sites from 'arm Y'. Arrows indicate 3'-end of DNA.

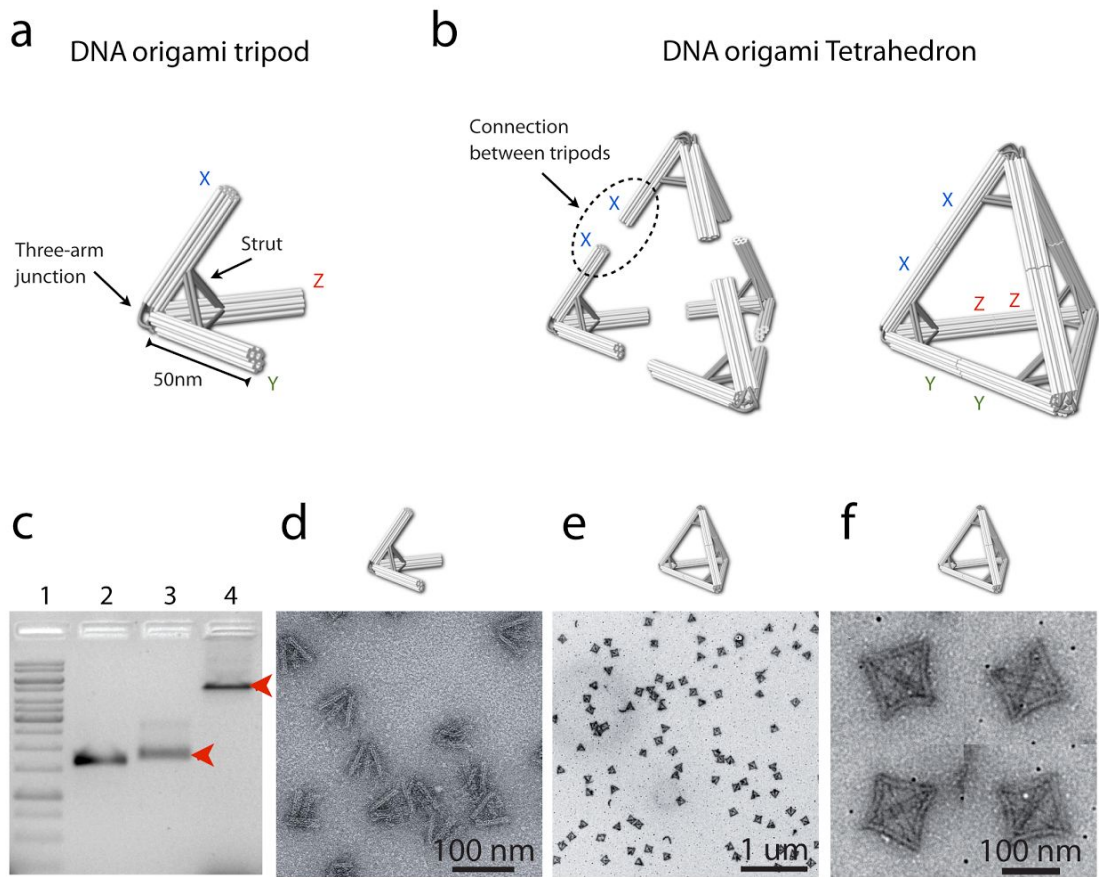


FIGURE S4. SELF-ASSEMBLY FOR TETRAHEDRON.

Three-arm tripod monomer design schematic. (b) Tetrahedron assembled from 60°-60°-60° DNA-origami tripod. (c) Agarose gel electrophoresis of the tetrahedron. Lane 1 is a 1-kb ladder. Lane 2 is the p7560 scaffold strand. Lane 3 is the 60°-60°-60° tripod monomer. Lane 4 is the tetrahedron (tripod trimer). Gel bands corresponding to desired products are marked by red arrowheads. Gel electrophoresis was performed using 1 % native agarose gels. (d) TEM images of the 60°-60°-60° tripod monomer. (e,f) TEM images of the assembled tetrahedron at two magnifications.

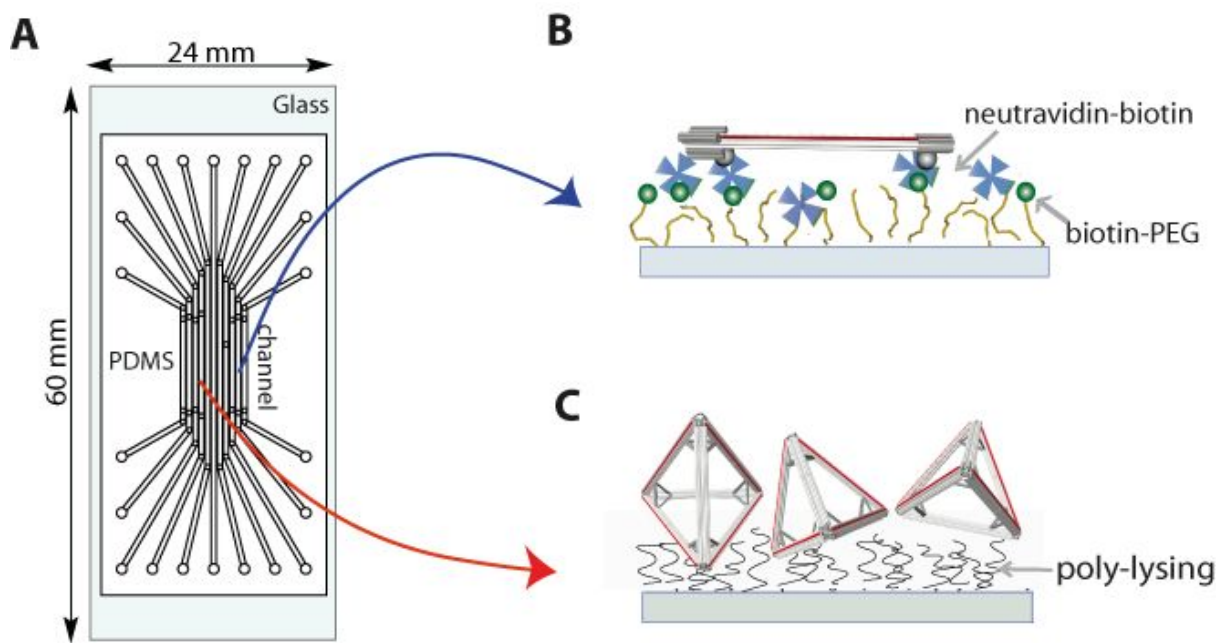


FIGURE S5. DNA-PAINT IMAGING OF DNA ORIGAMI IN MICROFLUIDICS CHAMBER

Scheme of experimental configuration for DNA-PAINT experiments (scheme is not at scale). (a) Microfluidics device was designed with 11 independent channels and a volume of ~5 μ l per channel. This design allows for several sequential experiments under different conditions. Injections and extraction of buffers and samples into the channels was performed using micropipettes or syringes. (b) Experimental configuration to immobilize linear rods. Linear rods contained biotin-labeled docking strands at its extremities. Biotin-neutravidin interactions were used to specifically attach linear rods to Biotin-silane-PEG/ Silane-P coated surfaces. (c) Tetrahedrons were immobilized onto poly-L-lysine coated channels to obtain random orientations with respect to the optical axis.

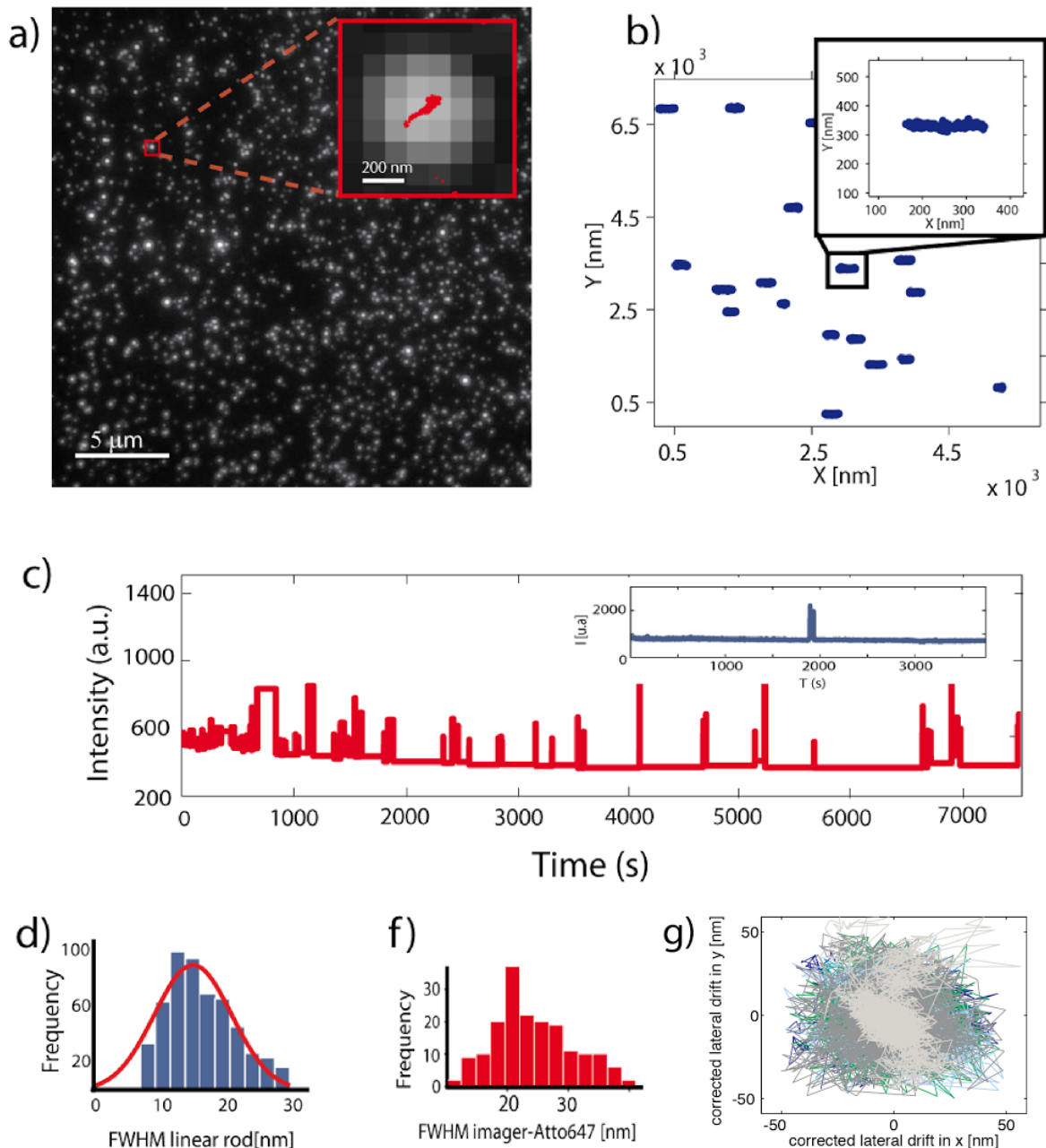


FIGURE S6. DNA-PAINT IMAGING OF LINEAR ROD

(a) Conventional TIRFM stack from DNA-PAINT experiment of linear rod labeled with oligo-Atto647n. Inset shows a magnified view of the stack with the localizations obtained from a single linear rod using a pointillist representation (red dots). (b) Magnification of selected linear rod localization clusters. Inset shows a further magnification. (c) Typical intensity versus time trace for linear rod. Transient binding between imager and docking strands produces fluorescence blinking, allowing stochastic super-resolution imaging. Inset: for comparison, the trace of a single imager strand binding to the surface in absence of origami. Estimations of localization precision: (d) distribution of FWHM of width profiles from linear rods, (e-f) Distributions of FWHM from localization clusters of single imager strands (e: Atto647n, f: Alexa488) attached non-specifically to a PEGylated surface with no DNA origami. The lower FWHM values in (f-g) versus (d) can be attributed to a smaller number of localizations possibly due to the shorter residence time of imager strands binding

non-specifically to the surface (e-f) as opposed to DNA origami (d). (g) Quantification of lateral displacement after drift correction. The lateral displacements of the different fiducial marks were recalculated after subtraction of the drift from the mean trajectory. The resulting standard deviations of the corrected trajectories represented here are $\sigma_x = 7.1$ nm and $\sigma_y = 8.6$ nm.

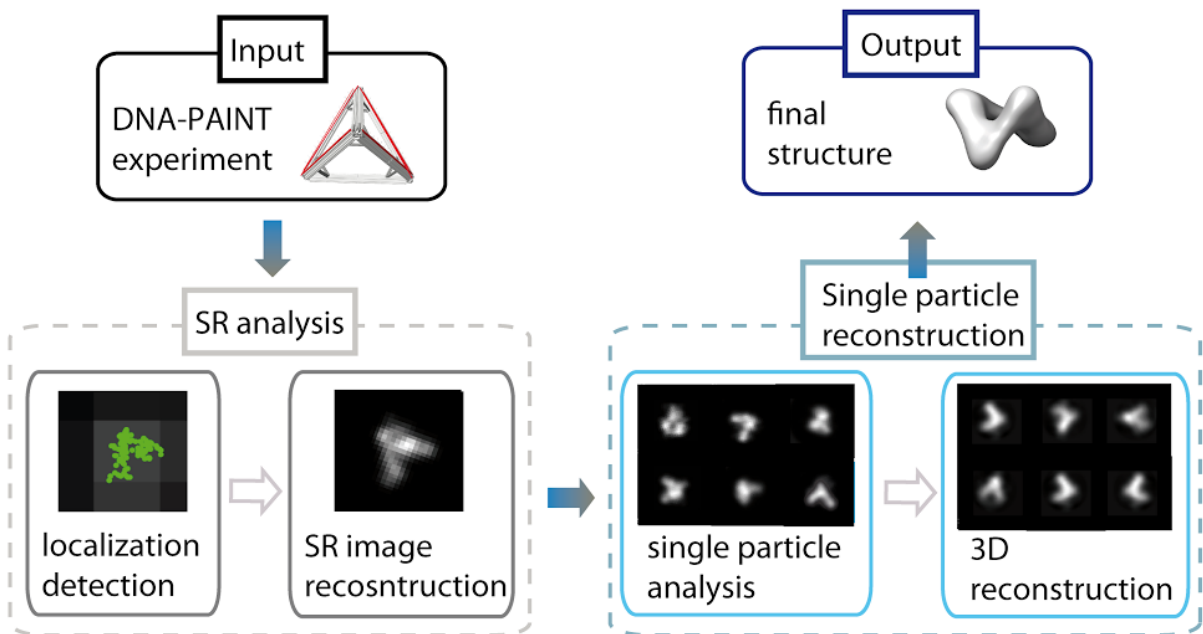


FIGURE S7. FLOWCHART OF FULL IMAGE PROCESSING

Our processing method is divided in two main cores: super resolution localization analysis and single-particle reconstruction. To begin, single-molecule events from DNA-PAINT experiments are detected and localized using MTT (1). Localizations are converted to a probability density reconstruction (SR image). Thousands of single probability density images are aligned, classified, and averaged using single-particle processing (see Figure S8) and used to obtain different projections of the particles. 3D reconstruction is performed to obtain a final 3D reconstruction.

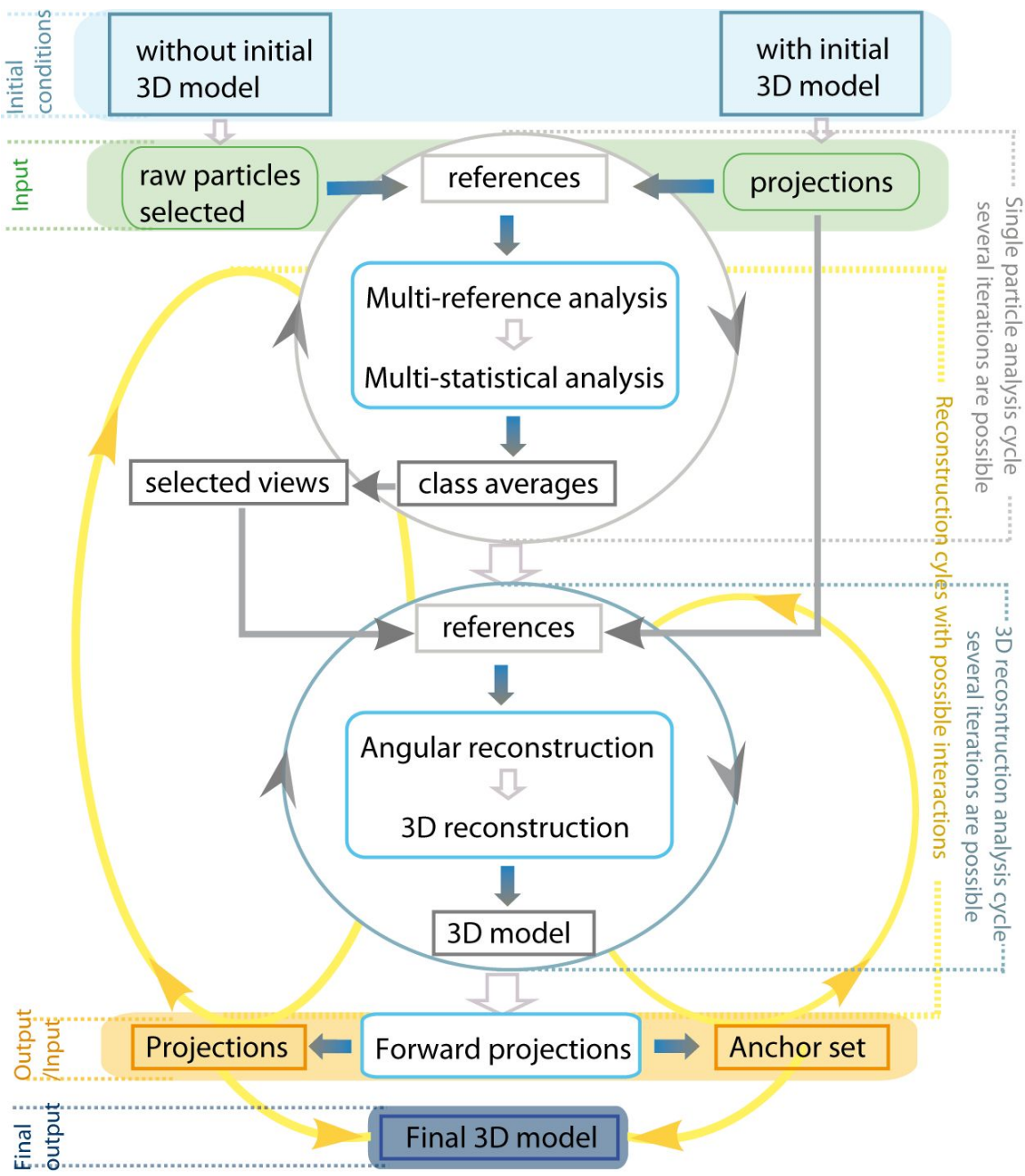


FIGURE S8. FLOWCHART OF THE GENERAL PROCESS OF SINGLE PARTICLE ANALYSIS (2D) AND RECONSTRUCTION PROCESS (3D)

Image processing can be divided in two parts, circles show main analysis processes, which are consecutive and iterative. The first part (gray circle) consists in image alignment and statistical analysis giving rise to class averages. The second step (blue circle) shows the basic steps in 3D reconstruction. Final 3D model (blue box) will be obtained after several cycles. Blue boxes show the key processing algorithm used.

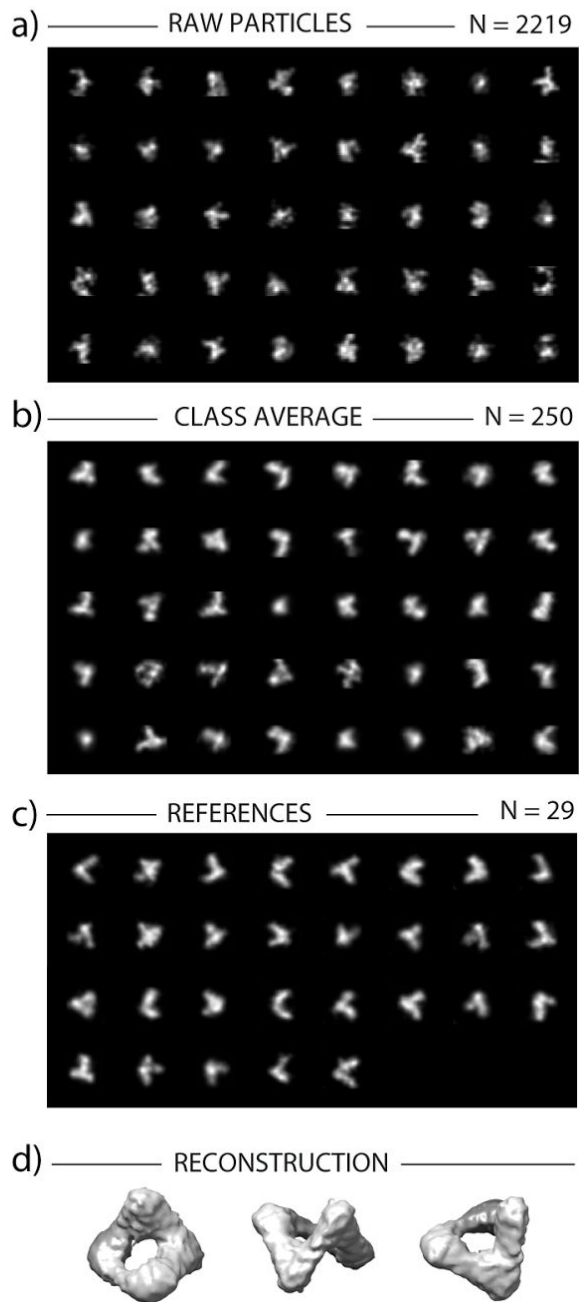


FIGURE S9. EXAMPLE OF PARTICLE AVERAGING METHOD IN DIFFERENT STEPS

Overview of image processing and 3D reconstruction of tetrahedron without initial model (unbiased reconstruction). Briefly, three class averages were selected corresponding to three projections of the origami with distinct orientations, *i.e.* different Euler angles. These selected class averages were used to assign Euler angles to all other class averages, and allowed computation of 3D reconstructions (see Online Methods for more details). (a) Representative images of input particles after centering, normalization and masking. (b) Subset of class averages obtained after multi-reference alignment and multivariate statistical classification of images corresponding to the second iteration. References for alignment were selected from initial class averages (no initial model was used). (c) References

(selection from best class averages) selected to perform the 3D reconstruction. (d) Final raw 3D structure obtained by angular reconstitution. C2 symmetry was applied.

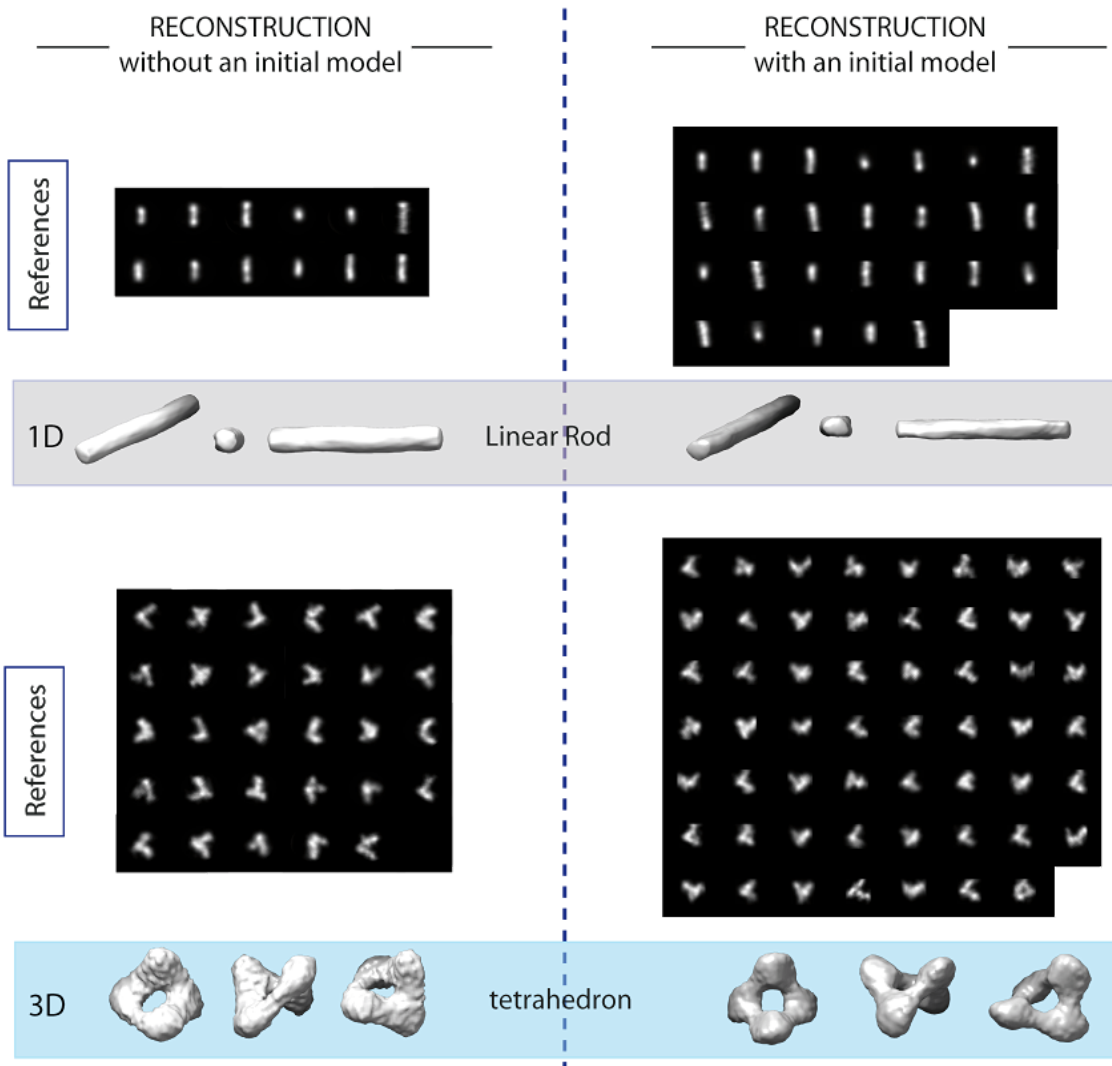


FIGURE S10. SELECTED REFERENCES AND UNBIASED AND BIASED 3D RECONSTRUCTION

Each panel presents class averages selected as references and the corresponding 3D volume reconstructed for reconstruction without (unbiased) and with (biased) an initial 3D model.

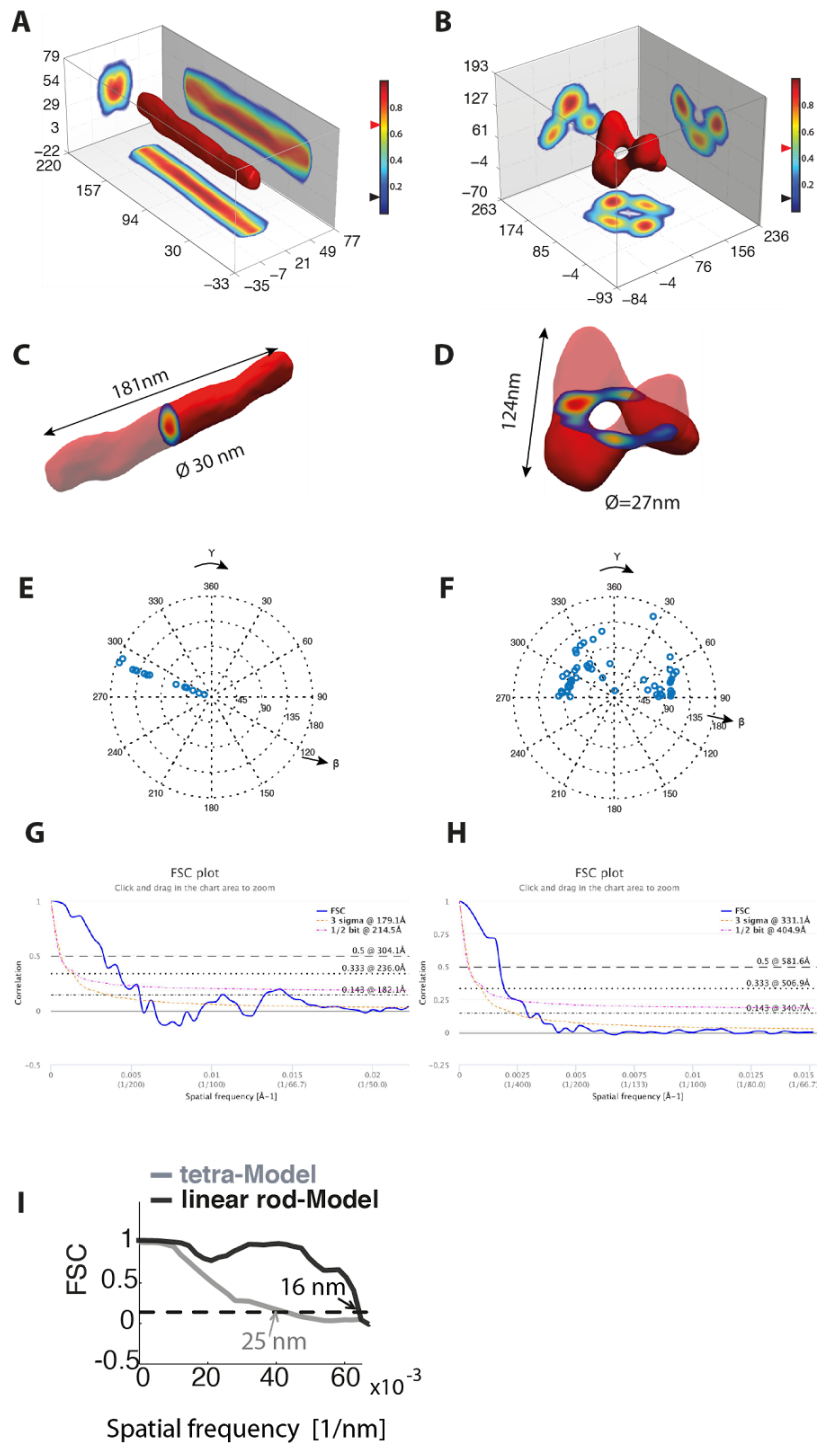


FIGURE S11. CHARACTERIZATION OF 3D RECONSTRUCTION WITH A REFERENCE (BIASED - RECONSTRUCTION)

(A-B) 3D structures for biased reconstructions of linear rod and tetrahedron. (c-d) Dimensions measured for both reconstructions. Black and red triangles on colormaps represent the threshold and iso values used for the intensity projections and 3D representation of the structures, respectively. (E-F) Euler angles distribution of the class averages used for the 3D reconstructions shown in (A-D). (G-H) Fourier Shell Correlation

(FSC) of the reconstructed structures against their respective models yielded 18 and 34 nm for the linear rod and tetrahedron, respectively (and 23.2 and 34.8 nm without initial reference). (I) FSC of the respective reconstructed structures (independent reconstructions from two halves of dataset).

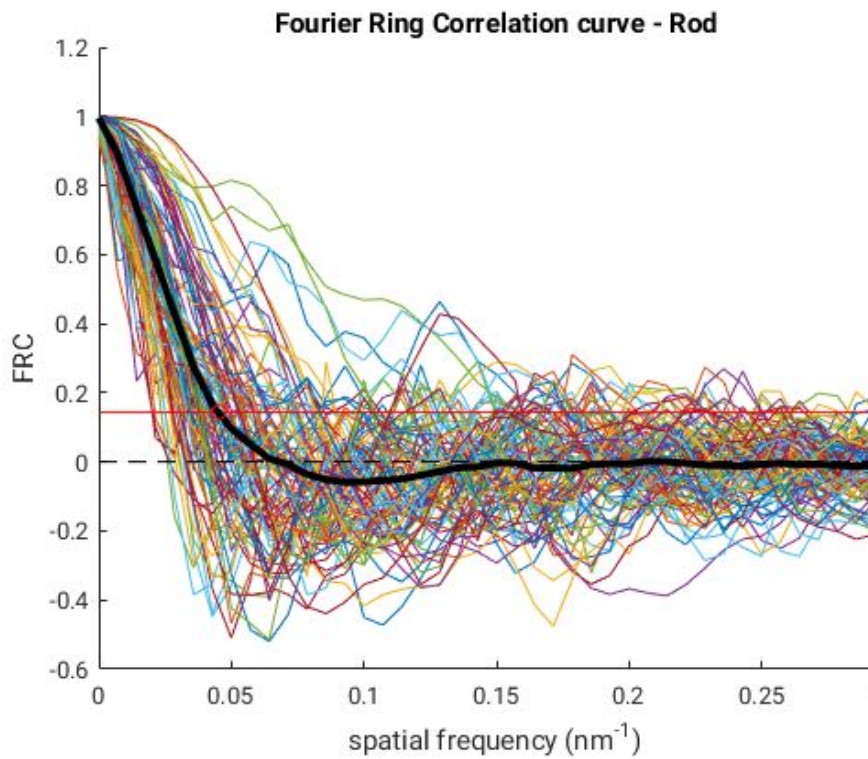


FIGURE S12. Fourier Ring Correlation of DNA-PAINT localization data

Application of Fourier Ring Correlation (FRC) to localizations obtained for single linear rods using DNA-PAINT (blue). To avoid spurious correlations due to localizations of a single emitter activation event, half data sets were obtained by splitting the time-series into blocks of 100 frames and assigning an equal number of blocks randomly to each half set (2). A subset of 100 origamis were randomly picked for display. The resulting mean curve (black thick line) crosses the threshold criteria (dashed red line at $1/7 \approx 0.143$) at a resolution of 22 ± 9 nm (mean +standard deviation).

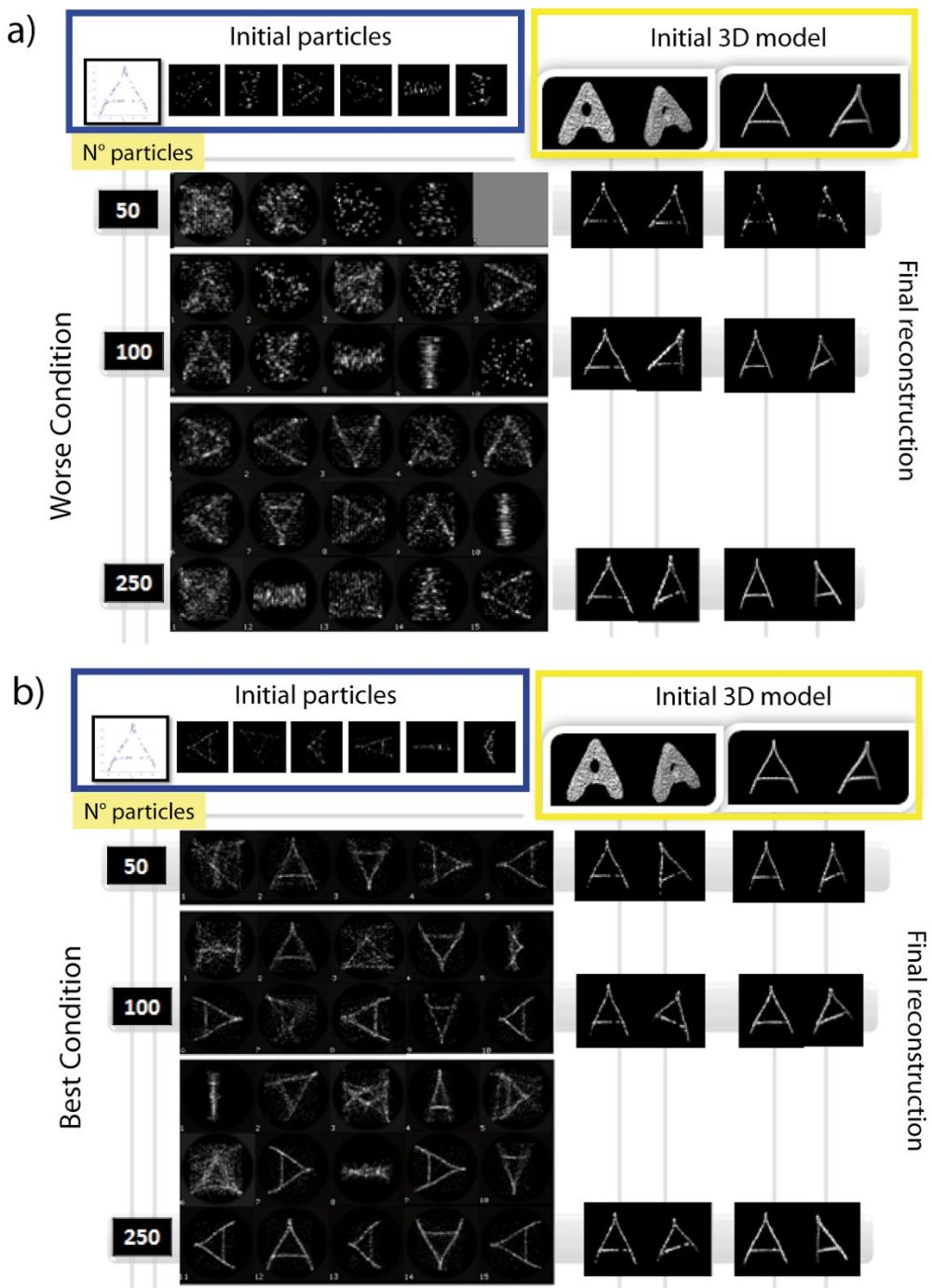


FIGURE S13. VALIDATION OF SINGLE-PARTICLE RECONSTRUCTION BY SIMULATIONS

The single-particle reconstruction method was validated by simulations. An origami with an 'A' shape was used as a model structure. DNA-PAINT experiments were simulated using different parameters, such as intensity (I), localization precision (p) of single localization events, total number of localizations per image (N_{loc}), percentage of background density (D_{bck}), and level of background intensity (I_{bck}). Different conditions were simulated: (1) **high** labeling density (200 localizations), **high** localization precision (10 nm), and **low** background (10% at 50 a.u.); (2) **low** labeling density (20 localizations), **low** localization precision (60

nm), and **high** background (20% at 90 a.u.); (3) **high** labeling density, **low** localization precision, and **low** background; (4) **high** labeling density, **high** localization precision, and **high** background. To simplify the presentation of results, only the first two conditions are presented: condition 2 (worst) in panel a and condition 1 (best) in panel b. Example probability density images derived from each condition are shown in blue boxes, whereas the two views of the model structure at two different resolutions are shown in yellow boxes. For each condition, different numbers of particles were simulated. This resulted in a number of class averages that increased with the total number of particles. Two types of 3D reconstructions were performed using low- or a high-resolution models from the theoretical structure (right columns).

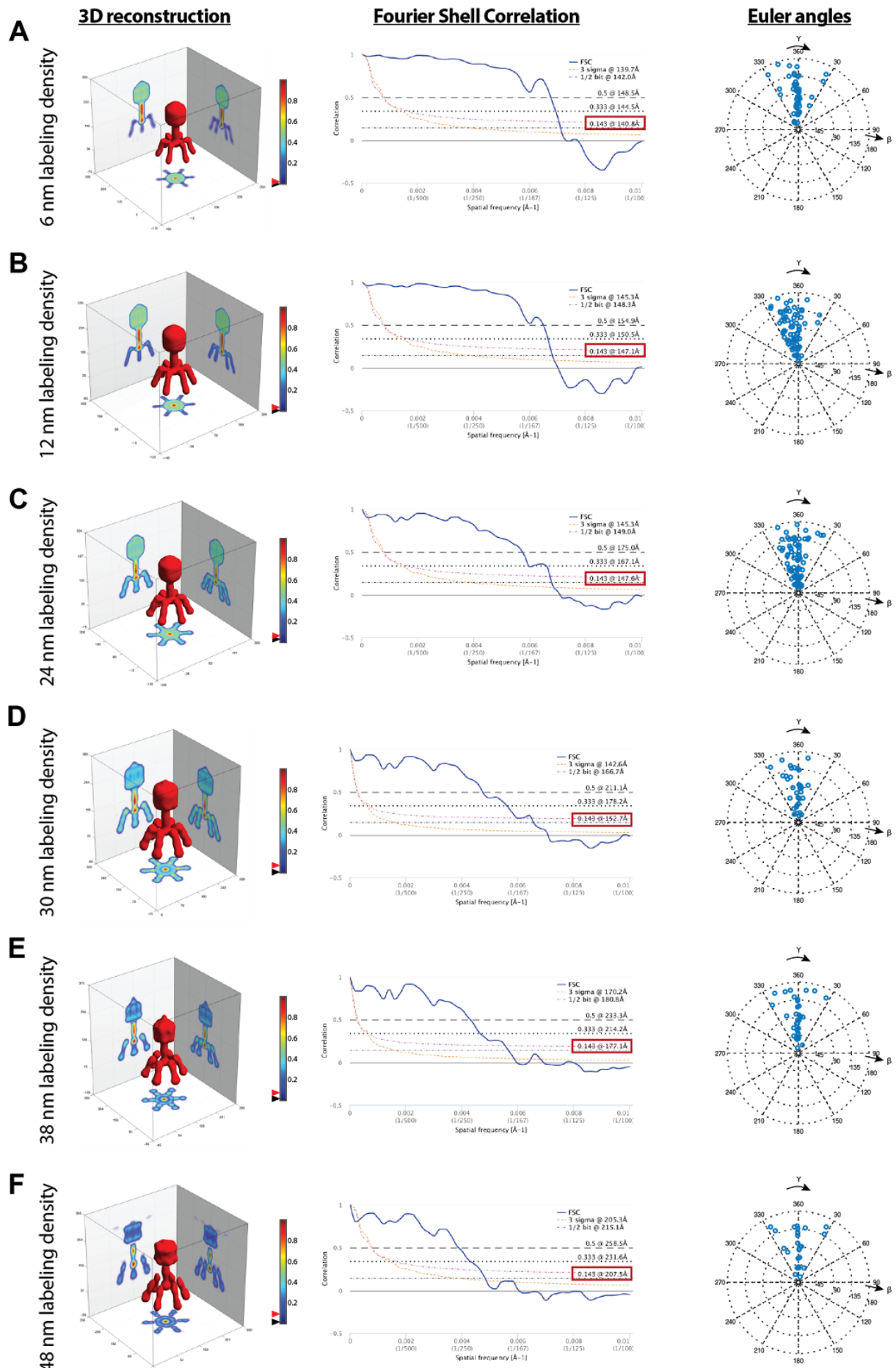


FIGURE S14. FOURIER SHELL CORRELATION OF BACTERIOPHAGE T4 RECONSTRUCTIONS FOR VARIOUS LABELING DENSITIES

3D single-particle reconstructions for different densities (shown on the left as a text column) are shown in left panels, whereas the corresponding FSC curves of the 3D reconstruction versus the high-resolution theoretical model are shown in middle panel (blue curves). Dashed horizontal lines represent different resolution criteria. In this study, we retrieved the spatial frequency at which the FSC signal dropped to 1/7 (0.14) to estimate resolution (see red square). Right panels: Euler angles distribution of the class averages used for each 3D reconstruction. Black and red triangles on colormaps represent the threshold and iso values used for the intensity projections and 3D representation of the structures, respectively.

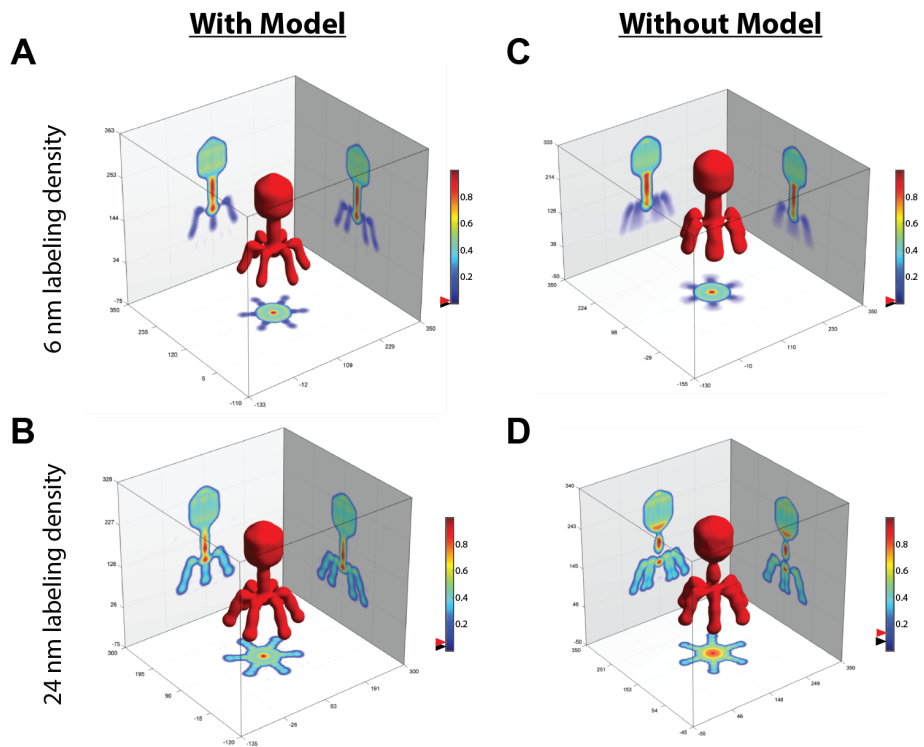


FIGURE S15. BACTERIOPHAGE T4 RECONSTRUCTIONS WITH AND WITHOUT MODEL

In Figure 3, single-particle 3D reconstructions were obtained by using a template (model) as a reference. The use of a template is more suited to objectively determine the effect of labeling density as it is not influenced by input from the user and represents the optimum reconstruction quality the user would otherwise achieve. However, we also tested whether 3D reconstructions could be obtained at different labeling densities from single-particle analysis without a template. Panels above display the final 3D reconstructions of the T4 bacteriophage with (A-B) or without template (C-D) at the same labeling densities. Notably, our method was equally able to reconstruct the structure without templates and even when the labeling density was lower than the localization precision. Black and red triangles on colormaps represent the threshold and iso values used for the intensity projections and 3D representation of the structures, respectively.

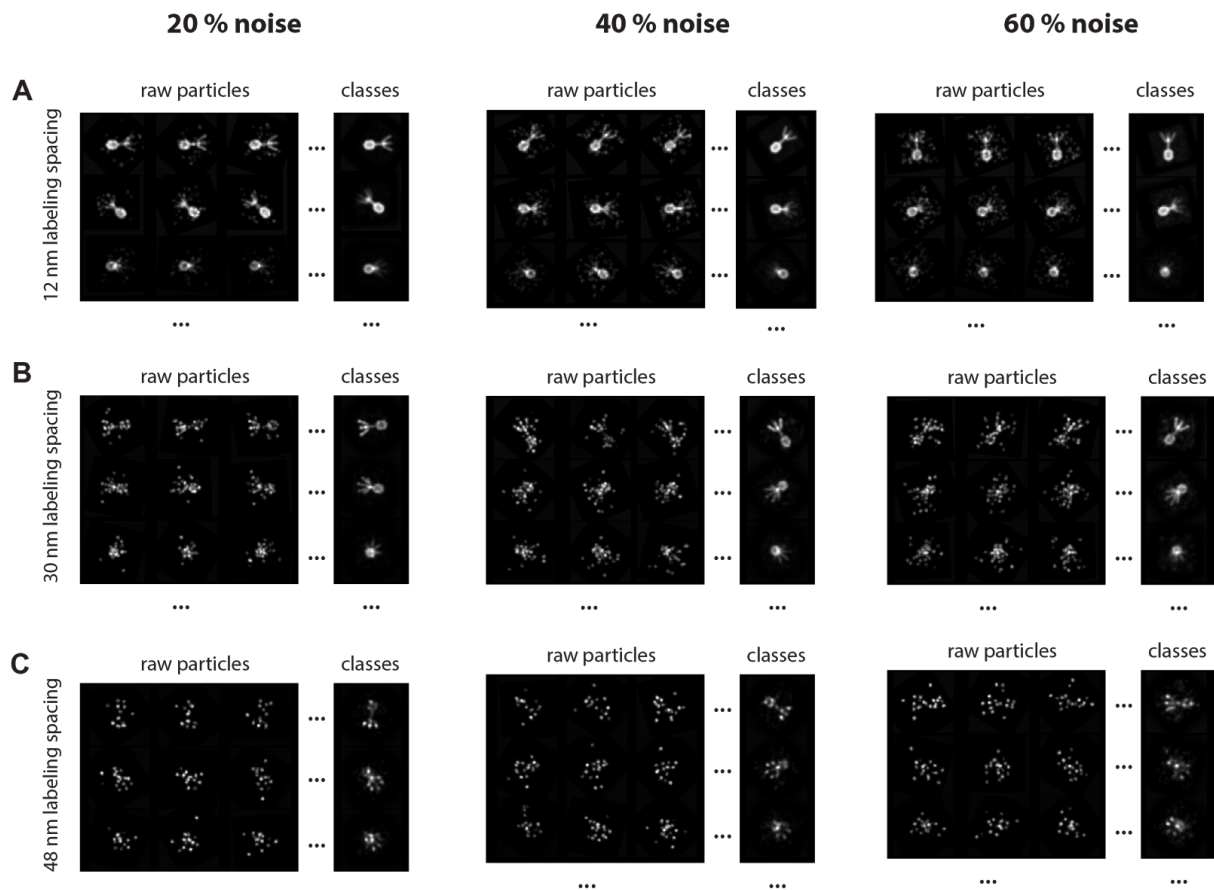


FIGURE S16. CLASS AVERAGES OF T4 SIMULATIONS AT VARIOUS LABELING DENSITIES WITH INCREASING NOISE CONTAMINATION LEVELS.

To test the effects of more realistic experimental conditions on the reconstruction process, we simulated and reconstructed datasets with different specific labeling densities (12, 30 and 48 nm in panels A, B and C) and increasing levels of contaminating background noise (20, 40 and 60% in columns left, middle and right, respectively). For each condition, 4000 raw particles with random orientations were simulated and classified into class averages by Multivariate Statistical Analysis (MSA) classification without any prior Multi-Reference Alignment (MRA). Well-defined class averages were then selected as references for MRA, followed by resubmission to MSA classification. The three most distinct class averages orientations are represented here for illustration. Note that a single cycle of MRA and MSA classification was employed here to show that the T4 structure can be retrieved in each case.

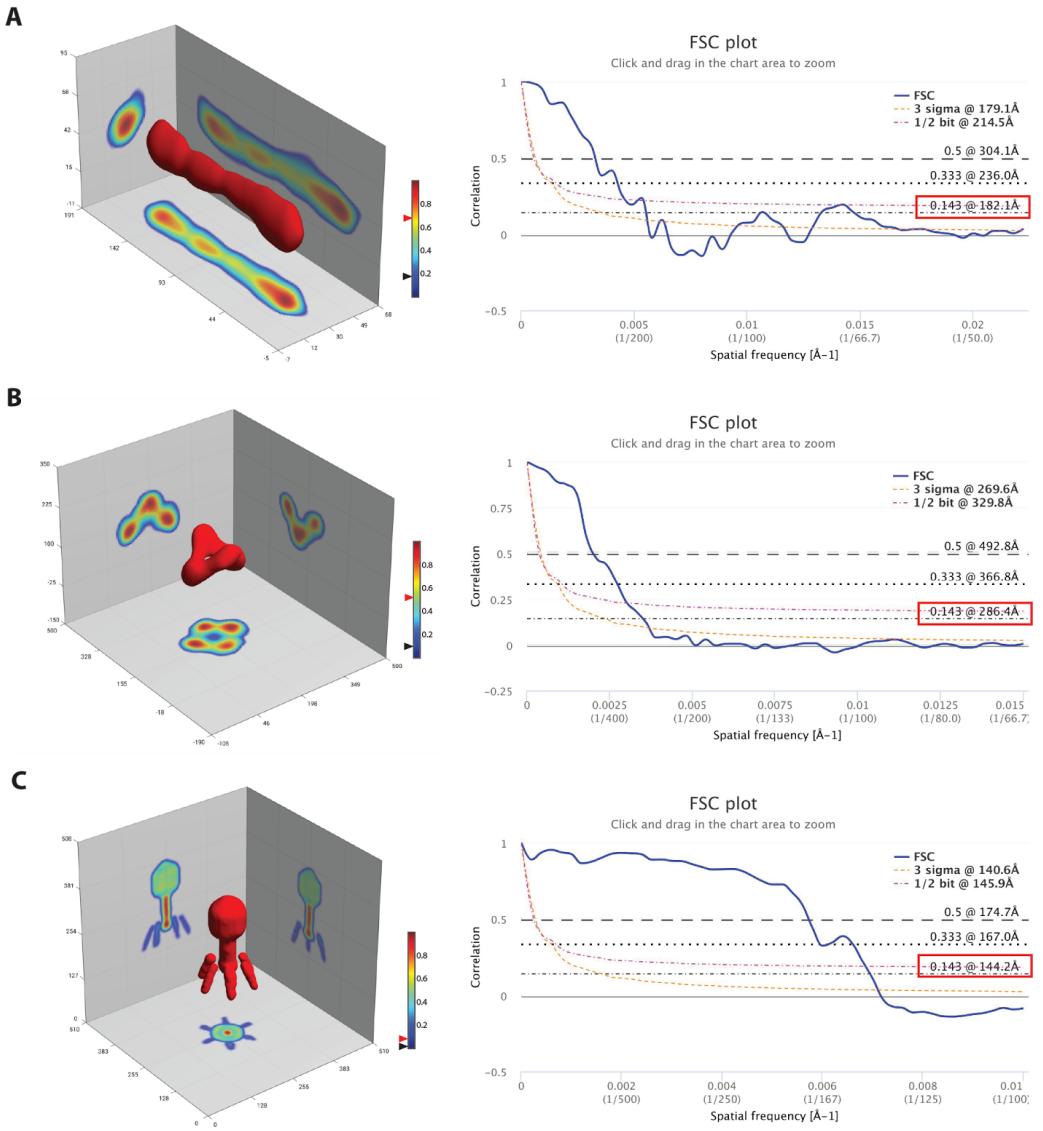
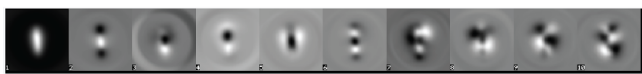


FIGURE S17. LINEAR ROD, TETRAHEDRON and BACTERIOPHAGE T4 RECONSTRUCTIONS WITHOUT SYMMETRY CONSTRAINTS

3D reconstructions of linear rod, tetrahedron and bacteriophage T4 structures shown in Figures 1, 2 and 3 were obtained by applying symmetries in the reconstruction process. To assess the robustness of the reconstructions in cases where the symmetry is not known, we reconstructed the same structures without applying symmetries (A, B and C, left panels). Linear rod and tetrahedron structures were obtained by using the same class averages as in Figure 1, while reconstruction of the bacteriophage T4 was obtained by using 1000 class averages (6 nm labeling density). Right panels show the FSC curves of the 3D reconstructions versus their respective high-resolution theoretical models to assess the fidelity of the reconstruction process. From these, we can extract resolutions of 18, 29 and 14 nm, respectively. Black and red triangles on colormaps represent the threshold and iso values used for the intensity projections and 3D representation of the structures, respectively.

A

Rod



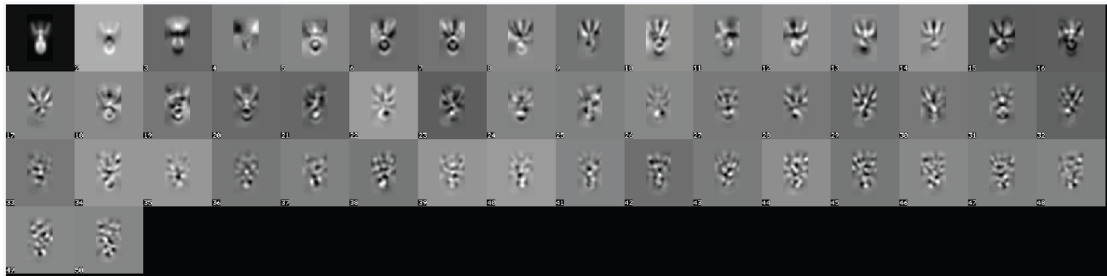
B

Tetrahedron



C

T4



D

Spirale



E

Duckling



FIGURE S18. EXAMPLES OF EIGEN IMAGES OF THE DIFFERENT STRUCTURES STUDIED IN THIS WORK.

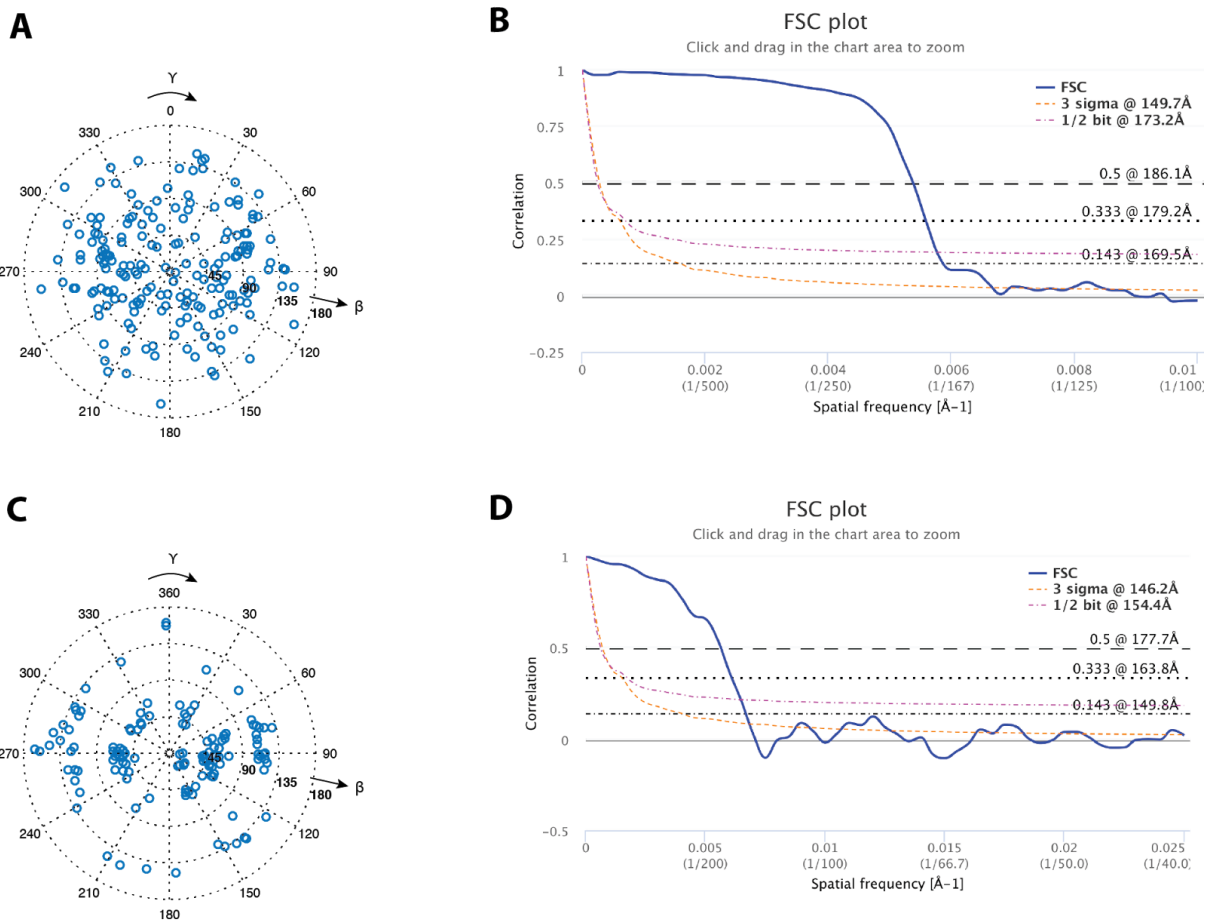


FIGURE S19. FSC AND EULER ANGLE DISTRIBUTIONS OF 3D RECONSTRUCTIONS OF ASYMMETRIC STRUCTURES

(A, C) Euler angle distributions of the class averages used for the 3D reconstructions in Fig. 4. (B, D) Reconstruction fidelity was estimated by calculating the FSC values between high-resolution models and final 3D reconstructions. We obtained 17 and 15 nm, respectively.

SUPPLEMENTARY TABLE 1. SEQUENCES OF LINEAR ROD STAPLES AND DOCKING STRANDS.

Sequence Virus-like	Color
TCTTTCCGAACAGAGCGAACCGCCCCGCCAGC	Core staple strands
AAAGCGCACTGTAGCGCTTCAACCTCCCAGAACCA	Core staple strands
TTCGACATGCGCAAGGAT	Core staple strands
TCAGGCCATTATACCAGAACTCGCTGACACCACGGAAATAAGTT	Core staple strands
ATATTCACAAACCCCCCTGCC	Core staple strands
CTTGAAATACCAAGAGCCATATAACCACAATCGGTTCCAGTCACGAC	Core staple strands
CGGTCTAATATGAATAATGGAAGGGT	Core staple strands
GAAACATTAGCTTACTTAGAA	Core staple strands
AACGAAAGAGGCATGAGGACGCGCCGAGGATAGCAGATAGG	Core staple strands
AAGTATAGCCCGGAGTAACGAAGAAAGGGTAAAGTACGGGCAACAGCTGA	Core staple strands
TTAGAGCTTGACGGCGAACGTGG	Core staple strands
TTATACTCTCAGAGAGGGTACGCGGAACAAGCCAGCT	Core staple strands
GGGCGCCAGGGTCCGGCAATTGTAGATCTAAGAATGTTCA	Core staple strands
CTCCAAGAAACACCAGTCAGTAAAAGCATTGGCAGATTCA	Core staple strands
ACCAAGACCGGAAGCAATCGAGCTCAAAGCGA	Core staple strands
GTTGAAACCTCAGGCGGTTAAAGGATTAAGGTGAATTA	Core staple strands
ATACACTAAAACACTCTAGCAACATGCCCATGGTTCAAGTGGAA	Core staple strands
CTCAGAGCCACCAAACCCATATTGTATGCCCAAATCCTGTTGAT	Core staple strands
GGCGCTAGGGCGCTGAAAAAGCGAAAGGAGC	Core staple strands
GGGGAGAGGCCTTTCGTCTTCATAACAGCGAACAGACGACGACAAT	Core staple strands
ACAGCAGATACATAAGGCCGTAATCAACCGTCTGTATTTAACCATTG	Core staple strands
CAATATCCACCAGCAGAATTAAAAATACCGAATTG	Core staple strands
ATTAACAATTCAATCAAGACCGGTATACGTCAAGCAGCGCTTCGCAC	Core staple strands
AGCTAAATAAGCAATAAATTGAGTAATGTGAGGTAAAG	Core staple strands
AGGGCGACATTCAATTCTTAGTTCCAATTGGAGAAACAATAACGG	Core staple strands
AAATCACAAAGGAACCTCATTTTATCAAACAT	Core staple strands
GTGAATAACCTGCACTAGAAAACGCTCCGCTACGCGGCTGGTAATGG	Core staple strands
CCCTTATTAGCGTTGCCA	Core staple strands
GGTCAGTGGTTATCCATTG	Core staple strands
CCTGAGAAAGTGTAGCTAAATGTGAGCGTTGCCAG	Core staple strands
TTTCAGAACGCCGAAAGACTAGCTTAATTCTG	Core staple strands
CCTTTTTAGGTTAAA	Core staple strands

AAATCCCTGAAACAGCCCGAAAACTCAATATTACGCCAGCC	Core staple strands
GATTTGTATCATCGAAGGGAACCGAACTAAGTCAGCTACCAT	Core staple strands
GGTCAATAGGTTGTTAAGTG	Core staple strands
GCAGATAGCCGAATATGCTTAAAAAATCTATAACACTTTAAT	Core staple strands
TTCCGGCACCGCTTAAAACGAGCTGCTGAAAGAGATAACATAAAG	Core staple strands
CACGCAAGGCAGCACCGCACATAATAATTAGAGCCAGCA	Core staple strands
GTAATAGCTTCGAACCTAACGAAATCGGCA	Core staple strands
GGAACAAACGGTGTAGATTGATAAAATTGGGGT	Core staple strands
CATTAGATACATATTGCATGGCTTGCAGGAAAGAAA	Core staple strands
CGGAGACAGTCAAATCAGCCAGTTGTAC	Core staple strands
ACTTAGACTTAATACATTGAGGAGAGCACTAAA	Core staple strands
GAACCAGAGCCACCACATAATCAAAATCAC	Core staple strands
GTCGGCGTGCATCTCAAAGGGAGCCCCGA	Core staple strands
CGCTACAGGGCGGCCACCGCGCTTAATGCGC	Core staple strands
AAAACCGTGAATAAAAAATCTATAATCCACGACCAGTAATA	Core staple strands
CCCAATTAAATGACCTTATAGTGCCAGAGGGGTAACCC	Core staple strands
ACATCGGGTTAACGTAGAAGTTGTGAGGGGATGTGCTGCAAGG	Core staple strands
GCCTGCCCGTAATAAGAATTAAAT	Core staple strands
TGCGTTGCGCTCACTGCCGCTTCTTAATGAGTAGCTGTATCG	Core staple strands
GGGTAGAATAATTGCGCTGGCCTTCTAGCGGG	Core staple strands
GAAAGTAGTAACAGAGAATGGGGTGCCAGTCGGGAAACCT	Core staple strands
TGGTAGCTGCGAACAGGTAGGATTAGACTAAATATCGCGT	Core staple strands
CAGCACTTATGGGATTITGCCGTTTGCCTATT	Core staple strands
CGTCAGAGTCTGGTCAGTCATAATTCTGTAAATCGCT	Core staple strands
AAAGCCTCAAAGAATTAGCAATAATCATACAGGCAA	Core staple strands
CGAGAAAGGAAGGGAAAGCAGGAAGATCAAGT	Core staple strands
GCTCAGTACCAAGGCTGAATTCTGTGACGACTGGAAACAGTACATAAA	Core staple strands
AAAAGATTAAGAGGAAAAAGCGGTTGCAAA	Core staple strands
TGGCATGCCTTCATAAGCCTATAATAATGCCATGAA	Core staple strands
CCTGCAGAACCTTCTCATATTCTTAATGCGCTCGGTTGT	Core staple strands
GTGAGTGTGTTCAATTCAACTTAGCAATGACCATATGGTTACCAAG	Core staple strands
CCGTTTCACGGTCATGCCAGAACGCCAGCGCAGTGTACG	Core staple strands
TCAGGTTAACATAGTAGCAATTACCTTGATCGGTGCG	Core staple strands

TCACCGTAAAAAAATCACAGAGCCTAAAATTATTCAATTCA	Core staple strands
GATAGCCCTAAAACGAGCAAGGAGCTAATTAGGAAAGGGGACTCGTAACATT	Core staple strands
CCCCTCAAAATGTCTAAATATTCTGCTCCATTAA	Core staple strands
AGAATCAATGCCCTAGAACCAATTCAATAAT	Core staple strands
ACATCCCCTAAAGGGTCAAATAAGCCTG	Core staple strands
GCCCCACGTAAACAAAACAACCAGAACATCCATTCTGGCCAACA	Core staple strands
ATTGTTCGCATTGTAACACTATGTAC	Core staple strands
GCACCAGCGTACTTAGACAAGAACGTTGGGA	Core staple strands
CGATTACCAGTCGGATCAAGGTGAACCGATTGA	Core staple strands
CAAGAAAACAAAATGCACCCAAATCAGAGGTCAGCCCAGCATCAGCGGGG	Core staple strands
CAAATATATTTAGCTCTGACCTAAGTTA	Core staple strands
CCAAGGCATTAAGAACCGAGAAACTATATGTAAATGCTGATGCAAATC	Core staple strands
CGCCAAGATAGTTAAAGACATGAAAATAACAGTACCTTT	Core staple strands
CCAGAGCCGACCCCTCAGAGCCACTCATCGGTAAA	Core staple strands
CCGTCAATAGATTACAAACAA	Core staple strands
GGGAAGGGCATGCGATGCTTGAGACGCATATGTCACAATCAATA	Core staple strands
AACAGAAAATAAGACATTAGACCATCACACTGGCTTGCCTGAACTGTT	Core staple strands
TTAATACTCCAACGAGTAGATTAGTTGAC	Core staple strands
AGTTAAAGGGAGAAAGATCCTCAGGACGTTGGCGG	Core staple strands
AAATGAACATCACCTAACAGT	Core staple strands
AAAAGGTATAGCGAACCGGCAAGTTTAATGCCGGA	Core staple strands
GGTGGTTATTCTGTACAGCGTGAAGAACGGGTATTAA	Core staple strands
ACCAGAGCTGAAAAGAACGCAATAACCTGTTAGCTATATTT	Core staple strands
AGTTTGAGTACATATTGAACAGTGCACGCATATCAA	Core staple strands
TGAGAGAAAAAGCCGTCGGATCGTAGAATATCCCATCCTA	Core staple strands
ATTCGGAACCTAGTTAATGAAATAAAACTCACATTAAAT	Core staple strands
TATAAACTTTTGTAATTCATCAGACCCCTG	Core staple strands
TCGGCCTCCATACGAGCCGGCCGTTCCAAAGTTGCCTTTAG	Core staple strands
GCCCCAGCAGCGAGCAGTTGCCGAAAAGTACCGAACATCGGCTGCTTT	Core staple strands
CAATGAGAGCAGCGGAACAAATTCAAT	Core staple strands
GTCCGTGAGCCTCCTGCGTGCTGTTCTC	Core staple strands
TTTCCGGCAACCTCCGATTAAG	Core staple strands
TGAGTAAACGACTGGTCTTATAGAACGCCTGTTATCAA	Core staple strands

AACAAAAGCCGGGGACCC	Core staple strands
ACCATTACCATTAGTGAGAATTCTAAAGCTATTTTAATTAC	Core staple strands
CCAATACTGCGGAATCAACTCCTTATTAC	Core staple strands
ATACCGACCGTGTGAGGATTTAATGGTTG	Core staple strands
AAAAGAGGAAACGAACAAAGTTACCCCTACCGCAC	Core staple strands
ATTACCTGAGCGTCTATTTCTGGAGGTGGAGC	Core staple strands
TAGAACAGGGTAAGTGTTCACGTTAAGTGGGCCGGAAACC	Core staple strands
CCCAAATATATTCAACAGGTATTTAGAAACCCCTT	Core staple strands
AGCGGCGGTCACTATTGATAAAACAGAGCTGACCT	Core staple strands
AGGCAAGGGAAGAGGGCTGCTAAAGGCCATATAAA	Core staple strands
GCTGGAGGTAGCAACCATGAAGGAACAACTCAGTAGC	Core staple strands
GATTAGGATTAGCGGGAGTGTGTACGGCAGCCAACGCGC	Core staple strands
ACCCCTAGAAGTATTTGCGGCTAAACAT	Core staple strands
GTCATGAGCTATCCTCATCACCCCTCCGCCTTTTCGGTCATAG	Core staple strands
CAGGTCAGACGATTCTCAGCCACCGGCTTG	Core staple strands
ATGGCTTAGAGTACGTTGATT	Core staple strands
ATTCGCCCAAATAGCCTTGCCTATGTTAAGTTGGGTAACG	Core staple strands
TATCACCGTACTCACAGACAGTTGCGAAGGCAGCCTTCACCGCCTGGCCC	Core staple strands
GGTTGCGGTATCACATCCCGTCGCTATGGCTCGTAATCAGTAGCG	Core staple strands
TGGATGATGGTTATCATACATTATAAAATCTTAGTTCAATCAATATCT	Core staple strands
GGTTTCTGCCAGCACCATGCACGCCGCAGTTGAGGACCGAGCTGAATT	Core staple strands
ACCACCAACCCGCATGGTCACGCTGCGCGTA	Core staple strands
CCCCCAGCGATTAAAGACAGTATTGGGAGTAGTTATAAGAACGTGGA	Core staple strands
GTGGCAACGCTGACCAACTTCATTCACTCAGTCTATCAGGGCGATG	Core staple strands
CTTGCCCGAACGTTACCACTCGTATTAAAGCATAA	Core staple strands
ATCGCAAGACATTGAGCTGTTCAAGAAATGTTAACGG	Core staple strands
TCAATAATCATATGCGTCTGTGATACAGGGTTT	Core staple strands
TATTCAGCCTTACTACCGTAATAAAACTTACAAA	Core staple strands
GCTGGCGAAAGGAGATAGGAAAAAGTGTGATACAGACAAA	Core staple strands
GGACGCTAATTCAATGCTTCGAAAG	Core staple strands
GAAAATTAACAACCGGCTACAGAGAGAATAACGTCA	Core staple strands
CTTCATCATCAATATGATATAGCACTAAATC	Core staple strands
CAGCGGTGCCGGTGTGCCGGTTACCTGC	Core staple strands

GCCGTCGAGAGGGGTCTTCCAGTTCTGCCGTGTTTCTTACCCAG	Core staple strands
ACAGAATAGTAAGCACTGGTAGTTAGTTATGTGA	Core staple strands
TAGCATTAACATGCATAGCGTATAAACTACTATGGTTGCTT	Core staple strands
GGCCTCTCGCAAATCATTGTGAATACTTCTACCTACATTGAA	Core staple strands
ATCGCGCAGAGGCCTTGCCACGAGAACACGGATAAACGAC	Core staple strands
CAAGAGTCACAAATTGGTTAAGAGCAAATTCTGCTGAAATGGA	Core staple strands
CACTACGAAGGCAGTGAGGAAAACAGCTAGACGCAATAAATC	Core staple strands
AAGAGAGATAATCGCAAATATTAAATTAAACGCCATCAAAC	Core staple strands
GCAAGCGGTCCACGTCGACATCCACGGGAAGCAAGAGCATGTAGAAACC	Core staple strands
CCAGGGTCGAAACGCTCATTCGGTTAAATATTGACGGAAAT	Core staple strands
AATTGTGTCGAAATGAGGCGCGAACGGTAATCAACTACGTGAACCATCA	Core staple strands
CATCAGACGATCTCGTCATAA	Core staple strands
ATCAAAATTATTGGAACACCCCCACCGAGGACGTTAGGCCATTGCCAT	Core staple strands
GTTTAAATATGCAACGTATGTTAGACTGGATAGC	Core staple strands
GCCAAAAGGAAACCCCTGTTACAC	Core staple strands
TAACAACGCCGTAATCACTGCGCTCTGGTGCTGCGACCGGG	Core staple strands
GGGAGGGAAAGGTATCAGCTGCAAGCCTCCAATCTGATTG	Core staple strands
GCTGAGACTCCTCATTAACGGGAATTAAAGCATAAGCTGCATTAATGAA	Core staple strands
TAGTACCGCCACCCCTACAACGCGTTGAATCCCGTAAGTTGCA	Core staple strands
TTTACAATAGGCCCTCATTCAGGGAAATACGTAATGC	Core staple strands
CGAGGTAGTAATCTTGAGATACAGGAGTAAGAACACGTGTT	Core staple strands
CACCAACTTCAACAGACGTGCTTAATTGAATTACCTT	Core staple strands
AAAAGAATAGCCGCTCACGACTTCTCATCACTCAGGAAAAACGCTC	Core staple strands
AAAATCATAGGTCTGACAATAGTGAATTATC	Core staple strands
TCATTGCGTGGTGTGCTGATAGCGGAGCAAGGCCGGAAACGT	Core staple strands
CAGAGTATGTTAGCAAACGTAGAAAAGACAGATAGA	Core staple strands
TCAATGCCGGACACGCCGTTAACAAATGAAACCATCGATAG	Core staple strands
AGAAAACGCAAAGAGGCCGTTAACAAATGAAACCACGCTAA	Core staple strands
CTCCATCAGTTGTATAAAGAAAAGCCCAAAGCGTCTGGAGCAAAC	Core staple strands
TTAATGCCGGAGGGCGTTGGAACGTCGCCGGCGC	Core staple strands
ACCAAGATTATCAGTATTAGATGCACAGACAATAACACCG	Core staple strands
TTGCCCTTAGTGGCAAGAACCCAAATATAAGCTCTGAACAA	Core staple strands
CGAGCCAGCAATAGCTATAGTGGCATCAATTCTACTAATAGTAG	Core staple strands

GCCACCCCTCAGAAAGTTCGAGGCTCCGTACACTGGTTT	Core staple strands
CGAAAAAAAAATCTCCCACCGACTTGAGCC	Core staple strands
GATGAATATACTAGTAGCAGCGTAATAACCGTGGTTATTACGCCA	Core staple strands
ACTAATAAAATCAACAGTCAGAAAAGGAAACCGACAGACGACGATAAAG	Core staple strands
AGACGGAATATAGTAAACTTACCGCTGAATTTGCGG	Core staple strands
CAATTGAGATTCTGTTTCTTGCAGGGCGGG	Core staple strands
GTCGTGCCAAGTGTATGTTATCACAGTAAAGAGAATATAAAG	Core staple strands
TATTTACCGATACTCGGAGGAAGCGAATTGCGTAGATT	Core staple strands
CATTTGGGGCGCAAATAGCGAACACTATCATATTA	Core staple strands
CGCGAAACAAAGTAGATCGTCAGGGAGTCCTGACGACGTCAAAGGGCGA	Core staple strands
ATTTGGGTTTCACCTGTAGCGCTAACGAGCAAA	Core staple strands
GATAGGTCAAGATCGCACTCCACATTATTTACCCAGTA	Core staple strands
CCCGGTTATCGATGAAAGGCTATCA	Core staple strands
GATCTACAACGGTAATCGT	Core staple strands
TCACTGTTGCCCTAATCCACACAACGACCAGTAAAAGGTAAAGTAA	Core staple strands
CGCAGACGACAGTATCGGTATCAGTTGACAATGGCTGAATTA	Core staple strands
GAAGATGATGAAACTGAATCTACCGCGTCCAACCCAGCTTACG	Core staple strands
GGCCAGTGCCAAGCTTCAGTGCCATCC	Core staple strands
ATTGACAGGAGGTTGAGG	Core staple strands
TATGACTTAATTAAACAACTAATAGATTAGAG	Core staple strands
CGGGTTGACTGTGACCGATTCTGAGGAATGGCAAATTGCTGAACCT	Biotin docking sites
CGGGTTGACTGTGACCGATTCTGCTCTGGTCATTATAATGCTGTAGCT	Biotin docking sites
CGGGTTGACTGTGACCGATTCTCATTCAAGTAAAGTACGGTGGAAATC	Biotin docking sites
CGGGTTGACTGTGACCGATTCTTCCCTGAGCTATTAAATAAA	Biotin docking sites
CGGGTTGACTGTGACCGATTCTCGGAACACAGAAGGCAGC	Biotin docking sites
CGGGTTGACTGTGACCGATTCTACGCTGAGAAGAGTGAGACTA	Biotin docking sites
GATCTACATATAATCAATCACTCATGTTACAAAACACTGCCGCCACC	DNA-PAINT docking sites
GATCTACATATAGAACAAACTATCGAGAACGTTAACCGG	DNA-PAINT docking sites
GATCTACATATTAAATGCAGAGCGGAAACAATGAAATAAAAGAACT	DNA-PAINT docking sites
GATCTACATATCAATAGAGCAAGCAGCTACAAAGTTAGCATAGGTG	DNA-PAINT docking sites
GATCTACATATCCAGTCAGTCAAGTGAGGCTGAACATTGCGGCAACGG	DNA-PAINT docking sites
GATCTACATATCAGTAATGGCTTACCGGAATGCCTGATTAAGAG	DNA-PAINT docking sites
GATCTACATATTAGGCAGTATTAAAGGCGTTAATAAACATTATTCT	DNA-PAINT docking sites

GATCTACATATGGAAATTGATTACTTACAGAGGCTAAAGA	DNA-PAINT docking sites
GATCTACATATTACCGACTAAAGCCAAAGCCTATAAGTTAGAGAAG	DNA-PAINT docking sites
GATCTACATATTTACGCCTTTTCCAGTACAAACTCAGAAC	DNA-PAINT docking sites
GATCTACATATTGCAATGCCTGAGTCAAAATTTCACAACTAA	DNA-PAINT docking sites
GATCTACATATTTAAGTCTGTCGGAGAGCAGCGATACCAAG	DNA-PAINT docking sites
GATCTACATATCGCTCAAAACCGTTAAACAGACGAGGGATTTGA	DNA-PAINT docking sites
GATCTACATATCAGAACGGGCTTATTAGTTGTTGTCTTGATAT	DNA-PAINT docking sites
GATCTACATATGAGATAGCAGGAACATAACCCCCGGAACCGCGAC	DNA-PAINT docking sites
GATCTACATATTCAAAAGGGTGACTCGTT	DNA-PAINT docking sites
GATCTACATATGAAAAATGAATCATTTACCAACATTCCAGGAGGTT	DNA-PAINT docking sites
GATCTACATATAAACACACCGCAGTTGAATAGTAAAGGATAAGT	DNA-PAINT docking sites
GATCTACATATAAAGGGACTGAGAATTGAGCGCAATCATCCTGATA	DNA-PAINT docking sites
GATCTACATATTCCTGCTATACAAATTCTGCCAGAGGAGCCGGG	DNA-PAINT docking sites
GATCTACATATGAAAGCGGCCGATTAAGCCCATTAAAG	DNA-PAINT docking sites
GATCTACATATCCTTATCATTCCGTAATATCC	DNA-PAINT docking sites

SUPPLEMENTARY TABLE 2. SEQUENCES OF TETRAHEDRON STAPLES AND DNA-PAINT DOCKING STRANDS.

Sequence Tetrahedron	Color
CTAGGCATCAATTCTGATCGCAAAAGTACGG	Core staple strands
GAATTAACAAACAAAGGCGT	Core staple strands
GCAGTTAGTACTGCGGAATCGTCAAATAGCGGAATTA	Core staple strands
CGGTCGCAGACTTTCAACCAGCCATGTAAGCCAGATTCTTG	Core staple strands
AACGAATTGCGTAGATTTGAATAATTTAT	Core staple strands
CTGAGAGAGTTGCCCTTCACCGCCTGGGG	Core staple strands
AGGGAAGAAAAGCCGTAAATGGGAT	Core staple strands
AACTAATGGAAGGGTTAGAACCTA	Core staple strands
TCATAGGGTATTAAGAACGCAGTATA	Core staple strands
TTAACACAACGCCATT	Core staple strands
GCCACCCCTCAGAGCCACCACCCCTCATAAAGATTCACTAAGTAA	Core staple strands
TATTCCTGATAGGCTATCAGGTCACTTTGAGACAGTATGTTGTT	Core staple strands
ATCGATGAACCGTAATCGTAAGTAGGTAAAGATTCAAAAG	Core staple strands
AAGGAAACCGAGGCCGAACAAAGTTACCAAG	Core staple strands
CCAAATAAGCTACACCAAGTTAATT	Core staple strands
GCTTAAGTGTATCGGGTGCCTAATGAGTAATGAATTCTTTAAA	Core staple strands
AGTAGAAGAACTCGAG	Core staple strands
AATCAATAGAAAAACA	Core staple strands
ACATAACCAGGTAGTTCAAGCATTCCAACGTTAGTCCAAA	Core staple strands
AAGTGTAGATTTAGCCCAAAT	Core staple strands
GCGTAAGGTTGAGTCATCAAAGAATAGGAGAGGCCGCGC	Core staple strands
CTATCGCGTAATAAAACC	Core staple strands
ATGACCATAAAAGCGAGCTCCTT	Core staple strands
AAATATGTTAGAGCAAAGACTTCAAATACTGA	Core staple strands
TCGGCTAACATGTACCGACA	Core staple strands
AAACATTATGACCCGTAAATATGTAACGTTAATATTTGTT	Core staple strands
GGCATTGAGAATAGCAAATGAGCCAGAGGCCGGAAAGTAAGC	Core staple strands
GAACGTGGCGAGAAAGGA	Core staple strands
GACAGGATTAGAAGTAAAATATCCTTATTGGAAATA	Core staple strands
TTAAGCATTAAACATCCACGAGCTGTTAGCTATGTTT	Core staple strands
GTGCGGCGGTGGGCCGGAAACTGTAGATG	Core staple strands
GGAAGTTATAACCGCAATGACA	Core staple strands

CCAGTTTTGGGTAAAGGGAGCCCCCGCGG	Core staple strands
AGTCAGAACGCAAGCCCGTTAATTG	Core staple strands
GTGAAATCTACGTGGCAGGCGTATTACATCAATAGCTTGAC	Core staple strands
CGAAAGGAGCGGGCAGCCGGCGGCCAC	Core staple strands
CGAGCGTGTACAAAGACGGGAGAATTAACGT?	Core staple strands
AACTACAAACGTATGGGAATTTTT	Core staple strands
AAATGATTAAGCCGCACTAACACATTGTCCTCAA	Core staple strands
GAGGCTGATTATCAGATGATGTGCTGGCAACTCCTGG	Core staple strands
TGTAGCACCATGCAATGGATAAAATCCGTGGTTTCGGCCAA	Core staple strands
GCAGGGCGAATAACTTCCCTT	Core staple strands
TGCACGAATATAGGGGCCTATGATATTGATGC	Core staple strands
AGAAAAAACGTACCAAAACCATTGGCGACA	Core staple strands
ATGCAGAGAAACCAGTACCGCCATCGGCTCAGTT	Core staple strands
CGCGTACAGAAGTGTAAACCGT	Core staple strands
TAAATAATTCATTTAACCTCCGGCTAGATTATAATGGACTCA	Core staple strands
GTAACCGGAACCTCGAGGT	Core staple strands
TCTGTTGAAATATCTGGATTTCGG	Core staple strands
GACATTCCAGACAATATTTTT	Core staple strands
TACATTAAACAAGTGAATTATCA	Core staple strands
TGTACTGGTAATAAGTTAAATGCCCTGCCTATTCGGA	Core staple strands
AAGAGCATGTTAGCAAACGCAA	Core staple strands
AGCCATACTTACCATCGCCTGATGAACCTTTAGAC	Core staple strands
TAATCAAATCACCGGAACCAGAACCGCCACCCCTCAGAGCCA	Core staple strands
GATCGTCCCGAACGCCCTCATAGTTAGCGTAAC	Core staple strands
GCTGAGAAGACTACCTTCTGACC	Core staple strands
GGAATAAACAAAAGGAATTACAGATATGAGAACATTACGA	Core staple strands
AGCAATAAAGACTCACATATA	Core staple strands
CTATTAAACCATCAAGCTTGACGGGGAGCTAGGGTGGGAACCATC	Core staple strands
CATTACCGCGCCCATTTCATCGTAGGAAC	Core staple strands
TTTAAAAGCGCAGTCTCTTCAATTACCGTAACCGTTAAT	Core staple strands
GATAAAATGTAATGCTACCTTATAGATTACGATTGGAGA	Core staple strands
GGACTAATGAGGCTTGATACCGATAGTTGAATAATATTGCTTT	Core staple strands
GAAATTAAATGTGAGCGAGTAAATGTTGGA	Core staple strands

TGTAATTTCTGAACAAAG	Core staple strands
AAAACGATAGTAAGGACGATAAAACCAATAA	Core staple strands
AGATAGAAACGCATTGTCAC	Core staple strands
ATCCCCGGGTACCAAA	Core staple strands
ACCGTCTATCAGGGCGAT	Core staple strands
AGTAATACCAGAACGATTACGCTGGTTGAGACGGCGTGCCAG	Core staple strands
ACAGTCAAATCAACCTGAAAGCGTCGAACTGA	Core staple strands
GAGAAGGTGTGAGTGAATTATAAAAAGC	Core staple strands
TCAACCAACCGTCGGACTGCCAGGAGTCCA	Core staple strands
ATCAAGTTGCCTTAGCGTTTAATAGCACGCCATA	Core staple strands
CCATATCAAAATTACAGATGAATATACACAAAGTC	Core staple strands
ATTATTAGCCAAAAGAGAGGGCTTGCAGTCCAAT	Core staple strands
TACGTGAAGAACGTTCGTAACACCGCTTTGGGAAGGCCAGTG	Core staple strands
GAGTACCTGATTGCAACGAGTGCAGTTGCAAGAACCGGATTGTA	Core staple strands
TTATACCGGTGCGGCCAGCTCGGCTGA	Core staple strands
CTTTAACCTCAATCAAGGAATTGTATCACCGGAGGGA	Core staple strands
GAATGGCTATTAGTCTTGATTGAGCAAGCACGGAGG	Core staple strands
AACTAGCATGTCAATCATATGTGTATAAGCAAATATTTAAAT	Core staple strands
GCCAAAGGTTTATTATAATAACGGAATATTA	Core staple strands
CTATCATAAATCTAACACCAGTCAGGACAAACAAAGCTTAA	Core staple strands
TTTACATCGGGAGAAACAATAACGGAACGCTAA	Core staple strands
TTAGCGTTGCCATCTTCAACCTATTATTCTGAAACATGA	Core staple strands
ATTGGAGACATGCCATTAAAAATGCCAGGTGTTGAAAACAGG	Core staple strands
TACAAACAATTGACAACTCGCTTGCTGAACCTCAAATATCA	Core staple strands
AAAACGCCGCAAATTITTTATAATCAGTGCGCCGCGATAAATACAA	Core staple strands
ATTGAGAAATAGCATT	Core staple strands
GTTTGAACAGTATGAGCAACACCGGA	Core staple strands
GCCCTTCCAAAAACACCAC	Core staple strands
TAAACAGGAGGCCAGAACATCAGAGCGGGACG	Core staple strands
TATTAATCCTTGCCTGAACAAACAAAGAAACCACCAAGAAGG	Core staple strands
CGGAGATCAACCTATCAACTTATACATTAGGAGGATCA	Core staple strands
AAACAATATAATTAGGACGTCAA	Core staple strands
ATTATTGCTTCAAACAAAGG	Core staple strands

TAGTAAAATGTTAGACT	Core staple strands
GCTTCAGGTCGCTAATATCAGAGGAATAACTCCAAT	Core staple strands
CCGCCAGATACTTCACGCCAGAACCTGTATGGTTGAT	Core staple strands
GCACGAAAACGACGGCGATTCT	Core staple strands
ATAATCGTACTCAGGAGAGCCAAGAACAAAC	Core staple strands
GAGCACGAACGGTTTGATT	Core staple strands
ACATTATCTATTAGACTAAAGTAT	Core staple strands
CTCGAATTCTCACTGCCGC	Core staple strands
CAGGGAAAATTGAGTTAACGTTTGACCCAGGCGGATAAGTGCCG	Core staple strands
AGATAGCAGCACCGTAAATTAGCACAAAATCTACCAGC	Core staple strands
TGAGTCATACAAAAATTGCGATTAAGCGGAGTTAAGAAAACGGGT	Core staple strands
CCAAGAACCAACCACAGAGGTCAAGAGTTGAATTCAT	Core staple strands
TGTATCGGTTATCAGCTTCCAAAATGTCGTCTTCAGCAGACAG	Core staple strands
ACAGTTCAAACCTCAAACAGCCCTGTTCTCAAATTAAA	Core staple strands
GAGATAGAGTAAAAGAGTCTG	Core staple strands
AGAGGGTGCCTTAATAAAC	Core staple strands
CCTCGTTGATTAAATTGCCTG	Core staple strands
AATCAAGGTTAGAAAATACAT	Core staple strands
CAGAGGTGAGGCGGTCACTATGAAAAATCTAAAGCATCAC	Core staple strands
CCTGCTCCATGTTAGAGTAATCTGAAGAATAGAAATCGCGA	Core staple strands
CATTACCTCAGTAGCGACAGA	Core staple strands
CAAGTTGGAACAATTGAGGCACTCCAGGCCTCTGTCACGAC	Core staple strands
ACAACCAGGAACACAGTTCAATTTCGTTCC	Core staple strands
GCAAGAGTCTGGAGCAATAATGCCGCCTACAAATACCC	Core staple strands
GGCTGAAACCCTCGACTGTAGCGCGTTTACTCATCAGAAGGCCAG	Core staple strands
AGTGAECTTGAATTCCGGCGTGCATTCTCCGCGCTGGC	Core staple strands
ACATAAATATTGACCATTAAATTAGCTCCATTCAAGAACCCCC	Core staple strands
AGTAAGCTATTACGTTCTGCCAATTGGGAAGAAAAGTCAGGATT	Core staple strands
TTCAACCGCAAAGGAACTGGCATGATTGCTA	Core staple strands
AGTTAAATACAGAGCCTGTAGGATA	Core staple strands
GGCCTTCAGAGGGTTGATATACCTCAGAACCGCCACCCCTCAGAAC	Core staple strands
AAATCATAGGTCTGAGAGAGTCATATTTCATT	Core staple strands
CCCCAGCGCCAACTTGAA	Core staple strands

TAGATAATCAACTAACGCGCAGGCTATT	Core staple strands
CTAATTGCCACTTCCAGAGC?	Core staple strands
CGGAAGCATAAAGTAGGGAGAGGCAGGTCAAGGCGATTGCG	Core staple strands
CTGTTACAAAGAACATGCTGATGCAAATCAATTAACTTGCTTCTGA	Core staple strands
CTCCGAATAACCCCCACCTTATGACAATGTAAGTTGAAAGGGGGATG	Core staple strands
ATCATAATTCAAATGGTTATATAACTATCTG	Core staple strands
ACCCATAAAATACATAGCGATAGCTTAGGTTGATATTT	Core staple strands
TCCATCATCATGGATTGACTCCGAAATGTTGCGTATTGGGACCG	Core staple strands
AAAGAAAAGATTGAGGTACCCGGTATTCTAAACCAAATCAATAA	Core staple strands
AGGTAAAGGTGGCACTTATTACGCAGTAAGAA	Core staple strands
AATCCCCACCAGACAGCAACA	Core staple strands
TGCACCCAGAAACGAGCCTTACAGAGAAGAT	Core staple strands
CACCAGAACGAGTCTGCCCTGACGAGATT	Core staple strands
CATTCGCCATTCAAGGCTGCGCAACTGCTGG	Core staple strands
AATAAACGTCTTCCTTATGTCGCTATTCAACCAGACGACGAC	Core staple strands
GTGGATGTTCTCTAAGTGTTCAGGAGAAGCCAGG	Core staple strands
AGTTAATGAATAAAAAGAAGAGATT	Core staple strands
GGCGCAGGACTCCAACGTCAAAGGGCGAAAA	Core staple strands
AACCACCAGCAGAAGATAAAAAGCGGAATTATCATCATATTC	Core staple strands
AACAGGTGAGAAAGGCCAACCGTCGCTGAAACAGGA	Core staple strands
TTTGCCAGAGGGGGTAA	Core staple strands
CTGTAGCCAGCTTAAACGGCGGATTGA	Core staple strands
AAAGGTATTCTTACCGAGGGCGGGTGAATAGGAAGGGATGAAAT	Core staple strands
GGATGGCCAACTAATGGTCAAGAGATGGCTGCTCACAGACCA	Core staple strands
CCCACGCTCCATTACTGGCTC	Core staple strands
AAAGATTAAGAGGAAAGCGGATTGCATCAA	Core staple strands
CTGATTCAATATAATACGCCACCTCAGGATCATT	Core staple strands
ACCGCCAAGTATAGAATAATTCGCGTCT	Core staple strands
AAGGCACTTGTATCGGAACGAGGCGCAGAGGCTGGTCAACGTAGA	Core staple strands
CGCAAGAGTATCATCCGACTT	Core staple strands
TAAGAGGCTGTAAAGAACCTCATGCGTTATACAAAAAGTAATTCTG	Core staple strands
CAAGGCCAAAGAATTAGCAATAAGGAGTAAATACACTAA	Core staple strands
GGCAGCCGCCAAAGCTAAATCGGTATTCTTGTGAATCACTACG	Core staple strands

CCTGAATTATTAATAAAAAA	Core staple strands
AGGTCACGTTGGCAGGCAAAGCGC	Core staple strands
CGCATTTACGCTCGCCTAGTGCTGATTTCCATCGC	Core staple strands
CATCAAACCCGGAATAGGTGTATCACGGACCAATAG	Core staple strands
AATACCACATITGAGATTAGG	Core staple strands
AAGCCAATAAAGTTCAGCTA	Core staple strands
CATGCCAGCATTACTAATAGTAGTAGCAATAA	Core staple strands
GCTTAATTGAGCCTGTTATCAACAATATCCTAAAGCAAGCCGTC	Core staple strands
GAACGCATTTCTTACAACGGCTTG	Core staple strands
CGAGGCAACTAACGTAGG	Core staple strands
TGGCTTTGATGATACAGGAGCCACCCCTCAGAGCCGCCACCA	Core staple strands
AAAAATAATATCCCAGATAAGAGGCAGA	Core staple strands
TACCGACC GTGTAATGGTTGAAA	Core staple strands
TGGGGCGATAAAATCATACAGG	Core staple strands
GCATGTAACGCGCCAGTAATA	Core staple strands
AGCCTCAACAAAGTTAATTAAACGAA	Core staple strands
AACACTCATTTCTGT	Core staple strands
ATATGGTTACCAAGTAGCAT	Core staple strands
AGGGTAGCAACGGCGCCGCTAGGTGAATTCTAGAAAATCTAAA	Core staple strands
GGATAGCAAAGAAGTGCAGAT	Core staple strands
GATCTAAAGTTGGAGCCTTAAT	Core staple strands
TTACCTCTAGCTGTACTCACATTAATTGAA CCTGTGCAACAGTAAT	Core staple strands
TCCGAATTAGTTAAATCAGCTCATAAACAAAGTTCGTTCATGA	Core staple strands
AATTCCAAATGAGTTGGTGGTGCTCAATTCTAGCTTACAGGG	Core staple strands
AGCTCAACATATTTCAAA	Core staple strands
AACACCCCTGAAGTAACAGTACCT	Core staple strands
TAAATTTGATAAATTCAAGAAAACAAAATTAAT	Core staple strands
ATCTATTCACAAAAGATCGGGACGACGAGATCTCGCTGC	Core staple strands
AACAGAACCCCTCTGCCATTGGCAAATATTA	Core staple strands
TTGATAAAAGTTCCATTAGTAATCATACCCAAACTGACCTT	Core staple strands
TAGCCCCACCCAGTTGCCCGAGTGCTTG	Core staple strands
AGAATCATGTAAACCGCGAGA	Core staple strands
GTAGAAAAACAGAAATAAGAAGCTAGCGGG	Core staple strands

GCCAAAACCTGACAATCCCTATAAGGGCTGGCGGGTAACG	Core staple strands
CAAGCGCAAAGAATTGGGTTAACCTGAAAAGGTTAT	Core staple strands
GTAAACATTAGTTAGAGGTTGAAGCTTAGGACAATAAT	Core staple strands
TGTCTGGGAGGTCTTAATTGAGCTTCATCAAAATTGA	Core staple strands
AGAGGCAGAAACAAATCATAAGGGAACCCGGTATTCACTGAAA	Core staple strands
AGAGAAATCGCTCAATTATCCGACTTGAGATCACACATACCGAA	Core staple strands
GGTCTTACCTCGCGTTTTGC	Core staple strands
GCGAAGAACATCGTGGCATGGCCAAACGACCCTTGCTG	Core staple strands
AAACTTTTACTAGTCATTCACAAAATTAGATTACCACAAGA	Core staple strands
GTAATATACATCACGGGATTAGACAGGTAT	Core staple strands
ATAACAGTTAATTACAGACCGGAAGCAGAAAACGCCT	Core staple strands
ATGGTCAGATAAAGGGTCCACCAGTCACCAGAGATGTGCTT	Core staple strands
CTTTGCGGGAGAACGCCTTATAAATGCAATGCCTGAGTAAT	Core staple strands
GCTTAATGAGGCCACCGAGCACTAAATCACCAACACGTAGCTATTGC	Core staple strands
CTGAATATAATGTGAC	Core staple strands
GATCTACATATTTGGTGTACAACACATACGACC	DNA-PAINT docking sites
GATCTACATATGTTGACTTAAGTGCCTGG	DNA-PAINT docking sites
GATCTACATATCTGCATTGAGCTATTCTGT	DNA-PAINT docking sites
GATCTACATATCGCGGAAGCCTGCGCTCAC	DNA-PAINT docking sites
GATCTACATATCCAGGGTATTGTCAGCTCTA	DNA-PAINT docking sites
GATCTACATATCCAAGCGTTGTAAACCGACA	DNA-PAINT docking sites
GATCTACATATAAGCAACTCGCCCTGCCATCTGT	DNA-PAINT docking sites
GATCTACATATCTTCCAGTCGGACGTTGCGCTAATC	DNA-PAINT docking sites
GATCTACATATAGAGGACAGATGAAGAACTGAATTATAC	DNA-PAINT docking sites
GATCTACATATGGCGCATACGGTCAAGTACAA	DNA-PAINT docking sites
GATCTACATATTACGTTAACAGCTTGCAGGG	DNA-PAINT docking sites
GATCTACATATAAAATACTGTGTCGAAATCCG	DNA-PAINT docking sites
GATCTACATATGAAAGACAGCATACCCCTCAGCAGC	DNA-PAINT docking sites
GATCTACATATCATCAACTTAGCCATCGCCT	DNA-PAINT docking sites
GATCTACATATAATTGCGCGCCGAATATATT	DNA-PAINT docking sites
GATCTACATATAAAAGGCCTTCGTTGCGG	DNA-PAINT docking sites

REFERENCES

1. Serge A, Bertaux N, Rigneault H, Marguet D (2008) Dynamic multiple-target tracing to probe spatiotemporal cartography of cell membranes. *Nat Methods* 5(8):687–694.
2. Nieuwenhuizen RPJ, et al. (2013) Measuring image resolution in optical nanoscopy. *Nat Methods* 10(6):557–562.